Rayleigh waves in micro-structured gyroscopic systems: Non-reciprocity and energy symmetry breaking

M. J. Nieves[1, *], G. Carta[2], V. Pagneux[3], and M. Brun[2]

[1] *Keele University, School of Computing and Mathematics, Keele, ST5 5BG, UK*

[2] *University of Cagliari, Department of Mechanical, Chemical and Materials Engineering, Cagliari, 09123, Italy*

[3] *Laboratoire d'Acoustique de l'Université du Maine (LAUM) - CNRS UMR 6613, Le Mans, 72085, France*

[*] Corresponding author: M.J. Nieves, email: m.nieves@keele.ac.uk

Abstract

Rayleigh waves are analysed in gyroscopic elastic systems. The in-plane vector problems of elasticity for a triangular lattice and its long-wavelength/ low-frequency continuum approximation are considered. The analytical procedure for the derivation of the Rayleigh dispersion relation is fully detailed and, remarkably, explicit solutions for the Rayleigh waves for both the discrete and continuous systems are found. The dispersion at low wavenumbers and the softening induced by the gyricity are shown. Despite of the symmetry of the dispersion curves with respect to the wavenumber, the presence of the gyroscopic effect breaks the symmetry of the eigenmodes and makes the system non-reciprocal. Such an uncommon effect is demonstrated in a set of numerical computations, where a point force applied on the boundary generates surface and bulk waves that do not propagate symmetrically from the source.

Keywords. Rayleigh waves, Mechanical metamaterial, Micro-structured elastic medium, Dispersion properties, Gyroscopic continuum, Energy flow.

1   Introduction

Rayleigh waves represent a special class of mechanical waves that are localised on the surface of a medium. Named after Lord Rayleigh (1885), who was the first to predict their existence, these waves travel along the free surface of and decay exponentially perpendicular to the boundary of the medium. Their speed of propagation is lower than the velocities of pressure and shear waves, propagating in the bulk. Indeed, when an earthquake occurs, Rayleigh waves are detected after the arrival of pressure and shear waves. On the other hand, these faster waves have smaller amplitudes than the slower Rayleigh waves, hence surface waves are usually more harmful than bulk waves.

1

In engineering, Rayleigh waves are of great importance and have diverse applications, ranging from material characterisation in non-destructive testing to mining exploration. In fact, Rayleigh waves are ubiquitous and arise in many scenarios that occur in the urban environment, including construction work, demolition, vehicular traffic and pedestrian movement. Further, Rayleigh waves play an important role in the design of electronic instruments that utilise piezo-electric materials capable of transforming mechanical energy to electric energy and vice versa. Examples involve sensors, filters and resonators amongst others. With regard to potentially enhancing these instruments, here we develop an elastic micro-structured device that exploits gyroscopic effects to control the flow of energy attributed to surface waves.

Rayleigh waves travelling on the surface of a linear elastic isotropic continuum have been studied in depth in the literature. The classical textbooks by Viktorov (1967), Achenbach (1973) and Graff (1975) are some examples of the many monographs on waves in elastic solids where the features of Rayleigh waves are discussed in great length. Nonetheless, the explicit form for the speed of propagation of Rayleigh waves, which depends on the Poisson's ratio of the material, is generally absent in textbooks. The determination of the velocity of Rayleigh waves was investigated in many papers, see for example the study by Hayes & Rivlin (1962). However, only relatively recently the expression for the speed of Rayleigh waves was provided explicitly by Rahman & Barber (1995) and, incidentally, we report here a compact form of this explicit solution. Chandrasekharaiah (1987) has studied the effects of voids on the propagation of Rayleigh waves in elastic half-spaces, whereas Liu et al. (1996) and Wang et al. (2019) considered the influence of cracks on these wave processes. In addition, the propagation of such surface states has been investigated for different types of media, for instance, see the work of Chiri & Ghiba (2012) for Cosserat materials, Akbarov & Ozisik (2003) for pre-stressed and Vinh & Giang (2010) for pre-strained materials. In addition, surfaces waves in anisotropic media and thermo-elastic have been studied by Vinh & Anh (2014), Vinh & Hue (2014) and Tomita & Shindo (1979), Abouelregal (2011), respectively. Rayleigh-type waves in materials with micro-structure and couple-stress effects were investigated by Georgiadis & Velgaki (2003). Nobili et al. (2020) have also considered surface resonances in thin plates in the framework of couple-stress elasticity.

In elastic media consisting of units that repeat periodically in space, surface waves are usually denoted as Rayleigh-Bloch waves. The existence of such waves and their connection with trapped modes in the presence of periodic gratings were analysed in scalar systems by Porter & Evans (1999), Linton & McIver (2002), Porter & Evans (2005) and Antonakakis et al. (2014). Similar analyses for plates have been tackled by Evans & Porter (2008), Haslinger et al. (2017), Morvaridi et al. (2018) and for in-plane vector elastic systems by Colquitt et al. (2015). In the context of electromagnetism, Rayleigh-Bloch waves propagating along linear arrays of spheres were examined in the work of Linton et al. (2013). Conversion of surface waves into bulk waves by means of rods with varying length, placed on an elastic half-space, was studied by Colombi et al. (2016), Colquitt et al. (2017) by developing the concept of the "resonant metawedge". In couple-stress elasticity, novel Rayleigh-like waves arise and they have been shown to be dispersive by Graff & Pao (1967), Gourgiotis et al. (2013) and Morini et al. (2013).

In discrete elastic systems, Rayleigh waves were analysed in the works of

Slepyan (2001), (2002), (2010) and Marder & Gross (1995) in the framework of dynamic fracture for uniform materials. The investigation of Slepyan (2001) describes how the angular velocity associated with Rayleigh waves varies with the wavenumber in a triangular lattice and shows the dispersive behaviour of surface waves in the discrete medium. Localised boundary waves propagating along crack faces in discrete systems may contribute to high crack face deformations, surface roughening and crack bridging (see the works by Mishuris & Slepyan (2014), Ayzenberg-Stepanenko et al. (2014) and Gorbushin & Mishuris (2018)). As shown by Nieves et al. (2013) and Piccolroaz et al. (2020), these effects can be suppressed or enhanced when anisotropy and dissimilarity are introduced into the lattice.

Further, we mention that the asymptotic treatment of surface and interfacial waves in elastic and flexural materials can provide greater insight into their behaviour as demonstrated in the survey conducted by Kaplunov & Prikazchikov (2017). Asymptotic approaches have also played an important role in modelling surface waves for coated elastic materials, which are of high practical importance in the design of composites for engineering applications. Some examples, where the analytical treatment of such problems can be found, include the work of Kaplunov et al. (2019), who considered interfacial resonances between an elastic half-space coated by a thin elastic layer with a clamped surface, and Fu et al. (2020), where surface resonances for anisotropic half-spaces with stratified and elastic coatings have been studied.

Here, we focus the attention on elastic gyroscopic systems, where the gyroscopic effect is produced by the mechanical action of gyroscopic spinners, that couple the in-plane displacements of the medium. The first model of a gyroscopic elastic lattice in which each nodal mass is connected to a gyroscopic spinner was proposed by Brun et al. (2012). The gyroscopic effect can be employed to tune the frequency at which dynamic anisotropy is observed, as shown in the work of Carta et al. (2014), to create extremely localised waveforms as demonstrated by Carta et al. (2017), to force waves to propagate along a preferential direction illustrated in the works of Nash et al. (2015), Süsstrunk & Huber (2015), Wang et al. (2015), Garau et al. (2018), Mitchell et al. (2018), Lee et al. (2018), Carta et al. (2019a), Garau et al. (2019), Carta et al. (2020) and to design cloaking devices to hide the presence of an object in continuous and discrete elastic systems. Concerning the latter, see the studies conducted by Brun et al. (2012) and Garau et al. (2019). Furthermore, Del Vescovo & Giorgio (2014) have shown that gyroscopic coupling can be used in the design of controlled smart structures that optimise the dissipation of mechanical vibration energy.

The analysis in Garau et al. (2019) was motivated by the need to understand the effective transient influence of a gyroscopic spinner on an elastic discrete system. An asymptotic analysis of the time-dependent equations, involving the combination of Euler equations for the gyroscopic spinner with the lattice's equations of motion, revealed that the gyroscopic coupling effect is dominated by a quantity called *gyricity*, which is the sum of the initial precession and spin rates. It is important to emphasize that the gyricity is a constant parameter, that is independent of the radian frequency of the lattice. A similar model was developed by Carta et al. (2018) and Nieves et al. (2018) to describe the coupling at the connection of an Euler-Bernoulli beam with a gyroscopic spinner. These recent analyses are relevant since they describe the dynamic behaviour of two-dimensional gyroscopic elastic systems. In particular, the dispersion curves
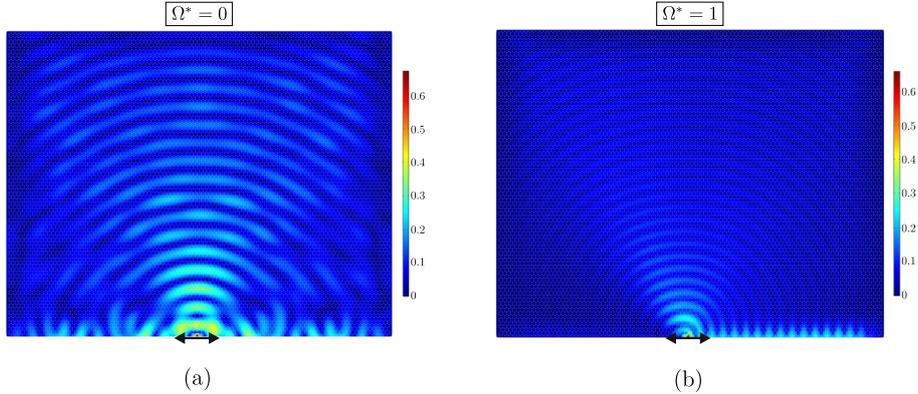
Figure 1: Total displacement amplitude field in the elastic lattice with (a) $\Omega^* = 0$ and (b) $\Omega^* = 1$, where Ω^* denotes the effective gyricity of the gyroscopic spinners, described in detail in Section 2. In each inset, the arrow indicates the time-harmonic force applied on the boundary of the medium.

remain symmetric with respect to the wavenumber components k_1 and k_2, and are parabolic in the low-wavenumber regime.

In this work, we analyse the propagation of Rayleigh waves on the free boundary of a two-dimensional gyroscopic elastic triangular lattice. We study the effect of the gyricity of the spinners on the dispersion curves and associated eigenmodes of the discrete system and we compare the results with a low-frequency asymptotic continuum model with distributed gyricity. The dispersion analysis developed for the discrete medium is also complemented with the numerical study of the behaviour of the lattice under an external force. The solutions to the forced problem show that gyricity can be used to break the symmetry in the response of the medium. This result is of paramount importance, as it can be exploited in engineering applications to design energy splitters, capable of channelling large amounts of energy along prescribed directions.

As an example, Figs. 1(a) and 1(b) illustrate the total displacement field in a forced lattice without and with gyroscopic spinners, respectively. In part (a), this field is clearly symmetric with respect to the point of application of the force. On the other hand, the presence of gyroscopic spinners in the system breaks the symmetry and induces preferential directionality in the medium, as shown in part (b).

The non-symmetric response of the lattice highlighted in Fig. 1(b) is linked to the non-reciprocity of the system due to the gyroscopic effect, which is formally demonstrated in the present paper. The idea of connecting gyroscopic spinners to a discrete system in order to generate unidirectional edge or interfacial waves has been proposed by Nash et al. (2015), Wang et al. (2015), Garau et al. (2018), Mitchell et al. (2018), Lee et al. (2018) and Garau et al. (2019) for hexagonal and kagome configurations. In the present paper, the mass points are arranged in a triangular lattice pattern and the attention is focused on Rayleigh surface waves. A similar analysis has been very recently proposed in the work of Zhao et al. (2020), who have simultaneously worked on a similar model. Here, after the analysis developed by Garau et al. (2019), we show that the non-reciprocity of the system cannot be linked to the lack of symmetry of the

Rayleigh dispersion curves, which remain symmetric, but to a different physical aspect. In fact, the analytical description of the waves propagating in opposite directions along the free boundary shows that their group velocities, namely the velocities of energy propagation, are the same, but the amplitudes and the elliptical trajectories of single masses are different.

We also report the work of Long et al. (2018) in which, exploiting the spin nature of longitudinal waves and the hybrid spin of mixed transverse-longitudinal waves, it is demonstrated that unidirectional Rayleigh waves can be produced by imposing circularly polarized elastic loads in elastic system with no gyricity. We note that such remarkable effect is not associated with non-reciprocity, but with the excitation of modes that propagate in different directions with opposite spins.

The paper is organised as follows. In Section 2, we present the formulation of the problem and we derive the explicit form of the dispersion relation for Rayleigh waves in a gyroscopic lattice. In Section 3, we discuss how the dispersive curves of the discrete system are affected by gyricity. Furthermore, we analyse the eigenmodes of the system and the displacements of the lattice particles as the wavelength and the gyricity are varied. In Section 4, we present the analysis for the continuum approximation of the gyroscopic lattice, and we compare the outcomes of the continuous and discrete systems. The formal demonstration of non-reciprocity is given for the continuum. In Section 5, we study numerically the response of the lattice to a concentrated force on the boundary and we demonstrate the non-symmetric propagation of the energy flow. Finally, in Section 6 we provide some concluding remarks.

2 Rayleigh waves in an elastic lattice attached to gyroscopic spinners

We consider an infinite two-dimensional array of particles with mass m, arranged in a triangular pattern. The particles are connected by elastic springs of stiffness γ and length L. Each particle is also connected to a gyroscopic spinner, as shown in Fig. 2(a), where the nutation, precession and spin angles are indicated by θ, ϕ and ψ, respectively. The gyroscopic spinner couples the displacement components in the x_1- and x_2-directions of the lattice particle to which it is attached. Here, it is assumed that the nutation angle of the gyroscopic spinner is small. All the gyroscopic spinners of the system are identical having length l, moments of inertia I_1 and I_0 (about the axis of revolution and the two perpendicular axes, respectively) and gyricity Ω. As derived analytically by Carta et al. (2018), Nieves et al. (2018), the gyricity is an independent constant parameter, given by the sum of the initial precession and spin rates, namely $\Omega = \dot{\phi} + \dot{\psi} = \text{Const}$.

2.1 Governing equations in the bulk of the semi-infinite medium

We start by analysing the bulk of the semi-infinite lattice, where each particle is identified by the multi-index $\boldsymbol{n} = (n_1, n_2)^{\mathrm{T}}$ (see Fig. 2(b)). Taking into account the assumption of small nutation angle, the equations of motion for the
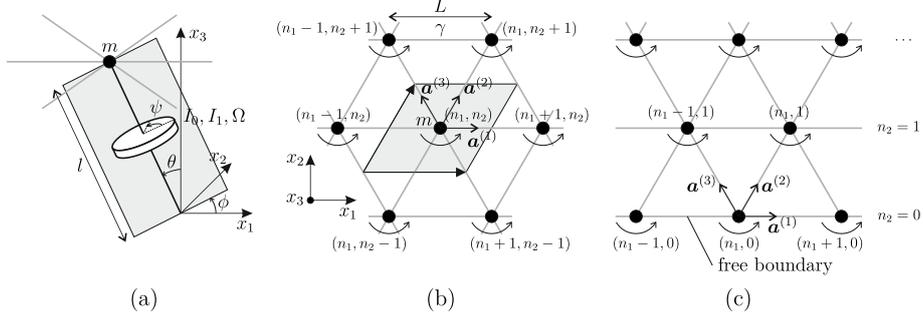
Figure 2: (a) Gyroscopic spinner, hinged at its base and attached to a lattice particle at its tip; the spinner's configuration is defined by the Euler angles θ, ϕ and ψ, representing the nutation, precession and spin angles, respectively. (b) Infinite periodic system, consisting of particles linked by elastic springs and connected to gyroscopic spinners. The grey area is the unit cell. (c) Semi-infinite lattice with a free boundary at $n_2 = 0$, supporting Rayleigh waves.

displacements of the lattice particles are expressed in linearised form following the study by Garau et al. (2019):

$$
\begin{aligned}
m^* \ddot{\boldsymbol{u}}^{(n_1,n_2)} = &- m^* \alpha \Omega \boldsymbol{R} \dot{\boldsymbol{u}}^{(n_1,n_2)} \\
&+ \gamma \Big[\boldsymbol{a}^{(1)} \cdot \Big(\boldsymbol{u}^{(n_1+1,n_2)} + \boldsymbol{u}^{(n_1-1,n_2)} - 2\boldsymbol{u}^{(n_1,n_2)} \Big) \boldsymbol{a}^{(1)} \\
&+ \boldsymbol{a}^{(2)} \cdot \Big(\boldsymbol{u}^{(n_1,n_2+1)} + \boldsymbol{u}^{(n_1,n_2-1)} - 2\boldsymbol{u}^{(n_1,n_2)} \Big) \boldsymbol{a}^{(2)} \\
&+ \boldsymbol{a}^{(3)} \cdot \Big(\boldsymbol{u}^{(n_1-1,n_2+1)} + \boldsymbol{u}^{(n_1+1,n_2-1)} - 2\boldsymbol{u}^{(n_1,n_2)} \Big) \boldsymbol{a}^{(3)} \Big] ,
\end{aligned}
\tag{1}
$$

where $\boldsymbol{u}^{(\boldsymbol{n})} = \boldsymbol{u}^{(\boldsymbol{n})}(t) = (u_1(t, \boldsymbol{n}), u_2(t, \boldsymbol{n}))^{\mathrm{T}}$ is the displacement vector (that is a function of time t) for the particle associated with the multi-index $\boldsymbol{n} = (n_1, n_2)^{\mathrm{T}}$, $m^* = m(1 + I_0/(ml^2))$ is the effective mass taking into account the spinner's contribution and $\alpha = I_1/(I_0 + ml^2)$. Moreover,

$$
\boldsymbol{a}^{(1)} = (1,0)^{\mathrm{T}}, \quad \boldsymbol{a}^{(2)} = (1/2, \sqrt{3}/2)^{\mathrm{T}}, \quad \boldsymbol{a}^{(3)} = (-1/2, \sqrt{3}/2)^{\mathrm{T}}, \tag{2}
$$

and

$$
\boldsymbol{R} = \begin{pmatrix} 0 & 1 \\ -1 & 0 \end{pmatrix} . \tag{3}
$$

In the time-harmonic regime, the displacement vector is given by

$$
\boldsymbol{u}^{(n_1,n_2)} = \boldsymbol{U}^{(n_1,n_2)} \mathrm{e}^{-\mathrm{i}\omega t} , \tag{4}
$$

where ω is the radian frequency and $\boldsymbol{U}^{(n_1,n_2)}$ is the complex amplitude to be determined.

Since we are interested in Rayleigh waves, we study the scenario where waves propagate along the boundary of the half-plane $n_2 \geq 0$ (see Fig. 2(c)) and decay in the direction perpendicular to the line $n_2 = 0$. Accordingly, we seek the displacement amplitudes in the form

$$
\boldsymbol{U}^{(n_1+p_1,p_2)} = \boldsymbol{U}^{(n_1,0)} \mathrm{e}^{\mathrm{i}(p_1+p_2/2)k_1 L} \Lambda^{p_2} , \tag{5}
$$

where $\boldsymbol{p} = (p_1, p_2)^{\mathrm{T}}$ is a multi-index and k_1 is the component of the wave vector associated with wave propagation in the x_1-direction. In addition, Λ is such that

6

$|\Lambda| < 1$ for $p_2 \geq 1$, allowing also for the case of complex Λ where exponential decrease in the wave amplitude can occur with oscillations.

Next, we introduce the normalisations

$$\boldsymbol{x} = \tilde{\boldsymbol{x}} L \,, \quad \boldsymbol{u} = \tilde{\boldsymbol{u}} L \,, \quad \boldsymbol{U} = \tilde{\boldsymbol{U}} L \,, \quad k_1 = \tilde{k}_1 / L \,,$$
$$t = \tilde{t} \sqrt{m^*/\gamma} \,, \quad \omega = \tilde{\omega} \sqrt{\gamma/m^*} \,, \quad \Omega = \tilde{\Omega} \sqrt{\gamma/m^*} \,, \tag{6}$$

where the tilde denotes a dimensionless quantity. In going forward we omit the symbol tilde for ease of notation and assume that all the variables appearing are dimensionless. Under these normalisations, the governing equations (1) in the time-harmonic regime become

$$\begin{aligned}
-\omega^2 \boldsymbol{U}^{(n_1,n_2)} = {}& \mathrm{i}\omega\,\alpha\Omega \boldsymbol{R}\boldsymbol{U}^{(n_1,n_2)} \\
& + \Big[\boldsymbol{a}^{(1)} \cdot \left(\boldsymbol{U}^{(n_1+1,n_2)} + \boldsymbol{U}^{(n_1-1,n_2)} - 2\boldsymbol{U}^{(n_1,n_2)} \right) \boldsymbol{a}^{(1)} \\
& + \boldsymbol{a}^{(2)} \cdot \left(\boldsymbol{U}^{(n_1,n_2+1)} + \boldsymbol{U}^{(n_1,n_2-1)} - 2\boldsymbol{U}^{(n_1,n_2)} \right) \boldsymbol{a}^{(2)} \\
& + \boldsymbol{a}^{(3)} \cdot \left(\boldsymbol{U}^{(n_1-1,n_2+1)} + \boldsymbol{U}^{(n_1+1,n_2-1)} - 2\boldsymbol{U}^{(n_1,n_2)} \right) \boldsymbol{a}^{(3)} \Big] \,.
\end{aligned} \tag{7}$$

2.2 Solution to the problem of surface waves in the bulk

Using (2) and (5), the governing equations (7) take the form of the homogeneous system

$$\boldsymbol{M}_1 \boldsymbol{U} = \boldsymbol{0} \,, \tag{8}$$

where

$$\boldsymbol{M}_1 = \begin{pmatrix} 5 - 4\cos^2\left(\frac{k_1}{2}\right) - \frac{1}{2}\left(\Lambda + \frac{1}{\Lambda}\right)\cos\left(\frac{k_1}{2}\right) - \omega^2 & -\mathrm{i}\Omega^*\omega - \mathrm{i}\frac{\sqrt{3}}{2}\left(\Lambda - \frac{1}{\Lambda}\right)\sin\left(\frac{k_1}{2}\right) \\ \mathrm{i}\Omega^*\omega - \mathrm{i}\frac{\sqrt{3}}{2}\left(\Lambda - \frac{1}{\Lambda}\right)\sin\left(\frac{k_1}{2}\right) & 3 - \frac{3}{2}\left(\Lambda + \frac{1}{\Lambda}\right)\cos\left(\frac{k_1}{2}\right) - \omega^2 \end{pmatrix} \,. \tag{9}$$

Here, $\Omega^* = \alpha\Omega$ denotes the "effective gyricity".

Non-trivial solutions of (8) are obtained by setting $\det \boldsymbol{M}_1 = 0$, which yields

$$\left(\Lambda + \frac{1}{\Lambda}\right)^2 + 4a\left(\Lambda + \frac{1}{\Lambda}\right) + 4b = 0 \,, \tag{10}$$

where

$$a = \cos\left(\frac{k_1}{2}\right)\left[\frac{2\omega^2}{3} - 1 - 2\sin^2\left(\frac{k_1}{2}\right)\right] \,,$$
$$b = \frac{\omega^2}{3}\left\{\omega^2 - 4\left[1 + \sin^2\left(\frac{k_1}{2}\right)\right] - (\Omega^*)^2\right\} + 1 + 3\sin^2\left(\frac{k_1}{2}\right) \,. \tag{11}$$

The biquadratic equation for Λ in (10) has four solutions. In view of the fact that solutions for Λ should take values inside the unit disk in the complex plane (see Eq. (5)), we can construct two solutions with this property as

$$\Lambda_j = \frac{\sqrt{g_j + 1} - \sqrt{g_j - 1}}{\sqrt{g_j + 1} + \sqrt{g_j - 1}} \,, \qquad j = 1, 2 \,, \tag{12}$$

where

$$g_j = -a + (-1)^{j-1}\sqrt{a^2 - b}\,, \qquad j = 1, 2\,. \tag{13}$$

The remaining solutions Λ_3, Λ_4 are found through $\Lambda_{j+2} = \Lambda_j^{-1}$, $j = 1, 2$.

For Λ_j $(j = 1, 2)$, we normalise the associated eigenvector $\boldsymbol{U}(\Lambda_j)$ such that

$$\boldsymbol{U}(\Lambda_j) = \begin{pmatrix} 1 \\ h_j \end{pmatrix}\,, \tag{14}$$

with

$$h_j = -\frac{\mathrm{i}\Omega^*\omega - \mathrm{i}\frac{\sqrt{3}}{2}\left(\Lambda_j - \frac{1}{\Lambda_j}\right)\sin\left(\frac{k_1}{2}\right)}{3 - \frac{3}{2}\left(\Lambda_j + \frac{1}{\Lambda_j}\right)\cos\left(\frac{k_1}{2}\right) - \omega^2}\,, \qquad j = 1, 2\,. \tag{15}$$

2.3 Surface waves along the boundary of the semi-infinite medium

Now, we concentrate on the unconstrained nodes along the free boundary of the semi-infinite lattice in Fig. 2(c), defined by $n_2 = 0$. In this case, the governing equations for the nodes along the boundary are

$$
\begin{aligned}
-\omega^2 \boldsymbol{U}^{(n_1,0)} = {}& \mathrm{i}\omega\,\Omega^* \boldsymbol{R}\boldsymbol{U}^{(n_1,0)} \\
& + \Big[\boldsymbol{a}^{(1)} \cdot \left(\boldsymbol{U}^{(n_1+1,0)} + \boldsymbol{U}^{(n_1-1,0)} - 2\boldsymbol{U}^{(n_1,0)}\right)\boldsymbol{a}^{(1)} \\
& + \boldsymbol{a}^{(2)} \cdot \left(\boldsymbol{U}^{(n_1,1)} - \boldsymbol{U}^{(n_1,0)}\right)\boldsymbol{a}^{(2)} \\
& + \boldsymbol{a}^{(3)} \cdot \left(\boldsymbol{U}^{(n_1-1,1)} - \boldsymbol{U}^{(n_1,0)}\right)\boldsymbol{a}^{(3)}\Big]\,, \qquad n_1 \in \mathbb{Z}\,.
\end{aligned}
\tag{16}
$$

Using the results of Section 2.1, the displacement amplitude vector for $n_2 > 0$ can be expressed by

$$\boldsymbol{U}^{(n_1,n_2)} = \boldsymbol{U}_0 \boldsymbol{\Lambda}^{n_2} \boldsymbol{C}\,, \tag{17}$$

where $\boldsymbol{C} = (C_1, C_2)^{\mathrm{T}}$,

$$\boldsymbol{U}_0 = (\boldsymbol{U}(\Lambda_1), \boldsymbol{U}(\Lambda_2)) \tag{18}$$

is a 2×2 matrix, and

$$\boldsymbol{\Lambda} = \mathrm{diag}(\Lambda_1, \Lambda_2)\,. \tag{19}$$

It remains to identify the condition for the non-trivial coefficients C_j, $j = 1, 2$, and simultaneously extend this representation to $n_2 = 0$ by satisfying (16).

The preceding solutions (17) satisfy the bulk equations (7). Hence, the equations (16) for the free boundary can be converted into a form that physically represents the vanishing of the two elastic forces below the node under consideration, namely:

$$\boldsymbol{a}^{(2)}\cdot\left(\mathrm{e}^{-\mathrm{i}k_1/2}\boldsymbol{U}^{(n_1,-1)} - \boldsymbol{U}^{(n_1,0)}\right)\boldsymbol{a}^{(2)} + \boldsymbol{a}^{(3)}\cdot\left(\mathrm{e}^{\mathrm{i}k_1/2}\boldsymbol{U}^{(n_1,-1)} - \boldsymbol{U}^{(n_1,0)}\right)\boldsymbol{a}^{(3)} = \boldsymbol{0}\,. \tag{20}$$

Substituting (17) into (20), we obtain the homogeneous system

$$\boldsymbol{M}_2\,\boldsymbol{C} = \boldsymbol{0}\,, \tag{21}$$

where

$$\boldsymbol{M}_2 = \begin{pmatrix} \frac{1}{\Lambda_1}\cos\left(\frac{k_1}{2}\right) - \mathrm{i}\frac{\sqrt{3}h_1}{\Lambda_1}\sin\left(\frac{k_1}{2}\right) - 1 & \frac{1}{\Lambda_2}\cos\left(\frac{k_1}{2}\right) - \mathrm{i}\frac{\sqrt{3}h_2}{\Lambda_2}\sin\left(\frac{k_1}{2}\right) - 1 \\ \frac{\sqrt{3}h_1}{\Lambda_1}\cos\left(\frac{k_1}{2}\right) - \frac{\mathrm{i}}{\Lambda_1}\sin\left(\frac{k_1}{2}\right) - \sqrt{3}h_1 & \frac{\sqrt{3}h_2}{\Lambda_2}\cos\left(\frac{k_1}{2}\right) - \frac{\mathrm{i}}{\Lambda_2}\sin\left(\frac{k_1}{2}\right) - \sqrt{3}h_2 \end{pmatrix}. \tag{22}$$

By imposing $\det \boldsymbol{M}_2 = 0$, we derive the equation

$$\sqrt{3}\left(h_1 - h_2\right)\left[\left(\Lambda_1 + \Lambda_2\right)\cos\left(\frac{k_1}{2}\right) - 1 - \Lambda_1\Lambda_2\right]$$
$$+ \mathrm{i}\sin\left(\frac{k_1}{2}\right)\left(\Lambda_1 - \Lambda_2\right)\left(1 - 3h_1 h_2\right) = 0. \tag{23}$$

The only acceptable solution of (23) is given by the explicit expression

$$\omega_{\mathrm{R}} = \sqrt{3\sin^2\left(\frac{k_1}{2}\right) + \frac{(\Omega^*)^2}{2} - \sqrt{\left[3\sin^2\left(\frac{k_1}{2}\right) + \frac{(\Omega^*)^2}{2}\right]^2 - 6\sin^4\left(\frac{k_1}{2}\right)}}, \quad (24)$$

which represents the dispersion relation for Rayleigh waves in the semi-infinite triangular lattice with gyroscopic spinners. We note that when $\Omega^* = 0$ the solution (24) coincides with the expression

$$\omega_{\mathrm{R}} = \sqrt{3 - \sqrt{3}}\left|\sin\left(\frac{k_1}{2}\right)\right|, \tag{25}$$

derived by Slepyan (2001) and (2002) for the analysis of Rayleigh waves in a triangular lattice without gyroscopic spinners.

3 Dispersion properties of Rayleigh waves in the semi-infinite gyroscopic lattice

3.1 Dispersion diagrams

The dispersion curves given by (24) are shown in Fig. 3 for different values of the effective gyricity Ω^*. In particular, the grey solid line represents the case when the effective gyricity is zero, while the black dotted, dashed and solid lines correspond to $\Omega^* = 1$, 2 and 3, respectively. All the curves are symmetric about the axis $k_1 = 0$ and 2π-periodic.

From Fig. 3 it can be noticed that the effective gyricity Ω^* induces dispersion at the origin. In particular, when $\Omega^* = 0$ the dispersion curve is linear at the origin with positive group velocity for $k_1 > 0$ and negative for $k_1 < 0$; when $\Omega^* \neq 0$, the behaviour is parabolic at the origin with group velocity equal to zero. This observation is confirmed by comparing the asymptotic approximations of (24) and (25) when $k_1 \to 0$, given by

$$\omega_{\mathrm{R}} \sim \frac{\sqrt{3 - \sqrt{3}}}{2}\left(k_1 - \frac{k_1^3}{24} + O(k_1^5)\right), \qquad \text{when} \quad \Omega^* = 0,$$
$$\omega_{\mathrm{R}} \sim \frac{\sqrt{3}}{2\sqrt{2}\Omega^*}k_1^2 - \frac{9 + (\Omega^*)^2}{8\sqrt{6}(\Omega^*)^3}k_1^4 + O(k_1^6), \qquad \text{when} \quad \Omega^* \neq 0. \tag{26}$$
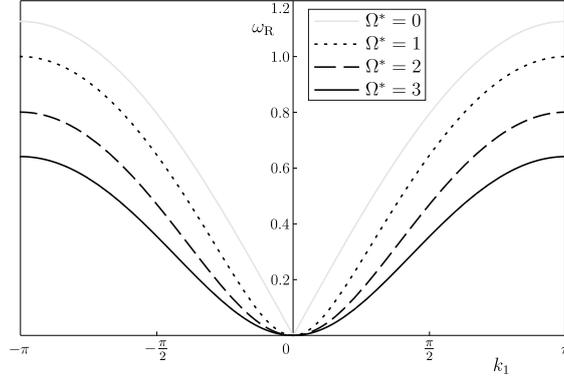
Figure 3: Dispersion curves associated with Rayleigh waves in semi-infinite elastic lattices, connected to gyroscopic spinners with different values of the effective gyricity Ω^*, specified in the inset.

In addition, we observe the softening effect of the gyricity with a reduction of the width of the pass-band as the effective gyricity is increased. For any value of Ω^*, the maximum of the dispersion curve is attained at $k_1 = \pi + 2n\pi$ ($n \in \mathbb{Z}$) and is given by

$$\max(\omega_{\mathrm{R}}) = \omega_{\mathrm{R}}(\pi + 2n\pi) = \sqrt{3 + \frac{(\Omega^*)^2}{2} - \sqrt{\left[3 + \frac{(\Omega^*)^2}{2}\right]^2 - 6}}\,, \qquad (27)$$

which is a monotonically decreasing function of Ω^*, with the limit $\max(\omega_{\mathrm{R}}) \to 0$, when $\Omega^* \to \infty$.

3.2 Eigenvectors and trajectories of the lattice particles

The eigenvector is calculated using (21). Without loss of generality, we take

$$\boldsymbol{C} = \begin{pmatrix} 1 \\ -\dfrac{\frac{1}{\Lambda_1}\cos\left(\frac{k_1}{2}\right) - \mathrm{i}\frac{\sqrt{3}h_1}{\Lambda_1}\sin\left(\frac{k_1}{2}\right) - 1}{\frac{1}{\Lambda_2}\cos\left(\frac{k_1}{2}\right) - \mathrm{i}\frac{\sqrt{3}h_2}{\Lambda_2}\sin\left(\frac{k_1}{2}\right) - 1} \end{pmatrix}\,. \qquad (28)$$

The horizontal and vertical displacements of a lattice particle on the free boundary are given by

$$u_j(t) = \mathrm{Re}\left(U_j \mathrm{e}^{-\mathrm{i}\omega_{\mathrm{R}}t}\right) = U_j^{\mathrm{R}}\cos\left(\omega_{\mathrm{R}}t\right) + U_j^{\mathrm{I}}\sin\left(\omega_{\mathrm{R}}t\right) \quad (j = 1, 2)\,, \qquad (29)$$

where $U_j^{\mathrm{R}} = \mathrm{Re}(U_j)$ and $U_j^{\mathrm{I}} = \mathrm{Im}(U_j)$.

From (29), we know that the trajectory of a lattice particle associated with Rayleigh waves is an ellipse. The canonical equation of an ellipse has the form

$$\frac{B_{11}x_1^2 - 2B_{12}x_1x_2 + B_{22}x_2^2}{\det \boldsymbol{B}} = 1\,, \qquad (30)$$

with a symmetric 2×2 matrix $\boldsymbol{B}$ to be now determined. Making use of (29), the components of the matrix $\boldsymbol{B} = \boldsymbol{B}^{\mathrm{T}}$ are expressed by (see also the study

in [Carta et al. (2019b)])

$$B_{11} = \left(U_2^{\mathrm{R}}\right)^2 + \left(U_2^{\mathrm{I}}\right)^2 = |U_2|^2\,,$$
$$B_{12} = -U_1^{\mathrm{R}}U_2^{\mathrm{R}} - U_1^{\mathrm{I}}U_2^{\mathrm{I}} = -\mathrm{Re}(U_1\bar{U}_2)\,, \tag{31}$$
$$B_{22} = \left(U_1^{\mathrm{R}}\right)^2 + \left(U_1^{\mathrm{I}}\right)^2 = |U_1|^2\,,$$

where $\bar{U}_2$ is the complex conjugate of U_2. The eigenvalues $\zeta_{\pm}$ and eigenvectors $\boldsymbol{Z}_{\pm}$ of $\boldsymbol{B}$ are given by

$$\zeta_{\pm} = \frac{\mathrm{tr}\,\boldsymbol{B} \pm \sqrt{\mathrm{tr}^2\boldsymbol{B} - 4\det\boldsymbol{B}}}{2\det\boldsymbol{B}} \tag{32}$$

and

$$\boldsymbol{Z}_{\pm} = \begin{pmatrix} \dfrac{B_{11} - B_{22} \pm \sqrt{\mathrm{tr}^2\boldsymbol{B} - 4\det\boldsymbol{B}}}{-2B_{12}} \\ 1 \end{pmatrix}\,, \tag{33}$$

respectively. Accordingly, the lengths of the minor and major semi-axes of the ellipse are calculated as

$$\xi_{\mp} = \frac{1}{\sqrt{\zeta_{\pm}}}\,. \tag{34}$$

The ratio of the length ξ_- of the minor semi-axis to the length ξ_+ of the major semi-axis is useful to determine the shape of the trajectory of a lattice particle on the free boundary. Of course, the ratio $\xi_-/\xi_+ \in [0,1]$. When $\xi_-/\xi_+ = 0$ the trajectory is a straight line, while when $\xi_-/\xi_+ = 1$ the trajectory becomes a circle.

Surprisingly, we have found that $B_{12} = 0$ for any value of the wavenumber k_1 and the effective gyricity Ω^*. Accordingly, the principal directions of the ellipse are aligned with the axes x_1 and x_2. We denote by ξ_1 and ξ_2 the lengths of the semi-axes along x_1 and x_2, respectively. Fig. 4 shows how the ratio ξ_1/ξ_2 depends on the wavenumber k_1, for different values of the effective gyricity Ω^*.

The solid grey line represents the case when the effective gyricity is zero. This curve is symmetric with respect to the axis $k_1 = 0$. The maximum value is reached at $k_1 = 2n\pi$ ($n \in \mathbb{Z}$) and is given by $\max(\xi_1/\xi_2)|_{\Omega^*=0} \simeq 0.68$, indicating that the motion of the masses in the ordinary lattice follows an elliptic trajectory with the major axis aligned with x_2. For $k_1 = \pi + 2n\pi$ ($n \in \mathbb{Z}$) the ratio $\xi_1/\xi_2 = 0$, which implies that the particle oscillates only along x_2.

The introduction of gyroscopic spinners into the system changes the behaviour of the medium dramatically. First of all, the curves cease to be symmetric with respect to the axis $k_1 = 0$. At $k_1 = 2n\pi$ ($n \in \mathbb{Z}$) we observe a jump in the ratio ξ_1/ξ_2 from 0 to approximately 1.22. For any value of Ω^*, there is a wavenumber for which $\xi_1/\xi_2 = 1$, corresponding to the case when the trajectory is a circle. The value of k_1 for which $\xi_1/\xi_2 = 1$ slowly varies with change of Ω^*; in the limit when $\Omega^* \to \infty$, $k_1 \simeq 0.432$.

4 Continuum approximation

We now inspect the continuous approximation of the preceding elastic lattice problem; it corresponds to the case where the wavelength is much larger than
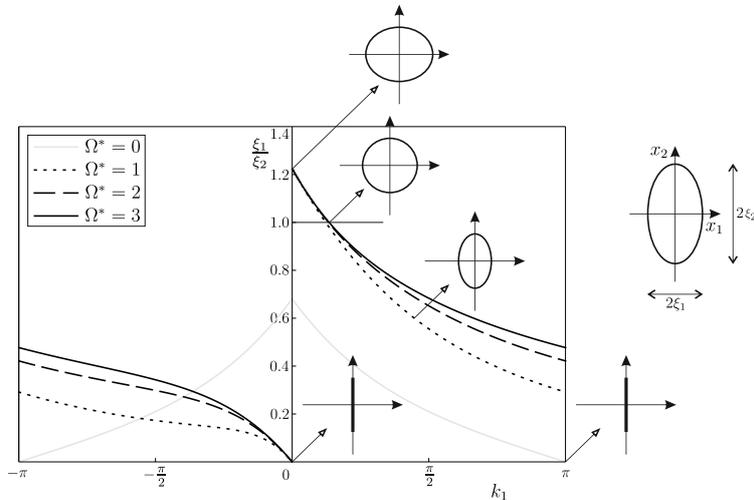
Figure 4: Ratio between the lengths of the semi-axes of the trajectory of a lattice particle situated on the free boundary, calculated as a function of the wavenumber k_1 and for different values of the effective gyricity Ω^*, specified in the diagram. Some instances of possible trajectories are included in the figure.

the distance between mass points. The objective is to get insights of the effect of gyricity on the classical Rayleigh surface wave.

In the low-wavenumber regime $k_1 \sim 0$, the equations of motion (1) are approximated by the continuous equations

$$\rho^* \ddot{\boldsymbol{u}} = (\lambda + \mu)\nabla(\nabla \cdot \boldsymbol{u}) + \mu \Delta \boldsymbol{u} - \rho^* \Omega^* \boldsymbol{R} \dot{\boldsymbol{u}} \,, \tag{35}$$

where, with a slight abuse of notation, $\boldsymbol{u} = (u_1, u_2)^T$ is now the displacement, which is a continuous function of the coordinate $\boldsymbol{x} = (x_1, x_2)^T$ and time t. Here, λ and μ are the Lamé moduli, ρ^* is the effective density, Ω^* the effective gyricity and $\boldsymbol{R}$ the rotation tensor defined in (3). The Lamé moduli and the density are related to the constants of the triangular lattice as follows:

$$\lambda = \mu = \frac{\sqrt{3}\gamma}{4s} \,, \quad \rho^* = \frac{2m^*}{\sqrt{3}L^2 s} \,, \tag{36}$$

with a Poisson's ratio $\nu = 0.25$ and out-of-plane thickness $s = 1$ m. We note that, except for the last term in (35), the asymptotic expression (35) is standard (see, for example, the work of Gonella & Ruzzene (2008)).

In the time-harmonic regime, with $\boldsymbol{u}(\boldsymbol{x}, t) = \boldsymbol{U}(\boldsymbol{x})\mathrm{e}^{-\mathrm{i}\omega t}$, (35) take the form

$$(\lambda + \mu)\nabla(\nabla \cdot \boldsymbol{U}) + \mu \Delta \boldsymbol{U} + \rho^* \omega^2 \boldsymbol{U} + \mathrm{i}\rho^* \Omega^* \omega \boldsymbol{R} \boldsymbol{U} = 0 \,, \tag{37}$$

where ω is the radian frequency, $\boldsymbol{U}(\boldsymbol{x})$ is the complex amplitude to be determined.

We introduce the in-plane volumetric deformation $\varepsilon^V = \nabla \cdot \boldsymbol{U}$, the in-plane clockwise rotation $\hat{\theta} = (U_{2,1} - U_{1,2})/2$ and the deviatoric part $\boldsymbol{\varepsilon}^D = \boldsymbol{\varepsilon} - \varepsilon^V \boldsymbol{I}/2$ of the deformation tensor

$$\boldsymbol{\varepsilon} = \frac{1}{2}\left(\nabla \boldsymbol{U} + \nabla \boldsymbol{U}^T\right) \,, \tag{38}$$

12

with $\boldsymbol{I}$ the identity tensor and $U_{i,j} = \partial U_i / \partial x_j$ $(i,j = 1,2)$. Then, *ad hoc* traces for the volumetric and deviatoric parts of (37) give the following equations

$$
\begin{aligned}
\left[\Delta + \left(\frac{\omega}{c_p} \right)^2 \right] \varepsilon^V &= 2 \frac{\mathrm{i}\Omega^* \omega}{c_p^2} \hat{\theta} \,, \\
\left[\Delta + \left(\frac{\omega}{c_s} \right)^2 \right] \hat{\theta} &= \frac{\mathrm{i}\Omega^* \omega}{2 c_s^2} \varepsilon^V
\end{aligned}
\tag{39}
$$

and

$$
\left[\Delta + \left(\frac{\omega}{c_s} \right)^2 \right] \varepsilon_{12}^D - \frac{\mathrm{i}\Omega^* \omega}{c_s^2} \varepsilon_{11}^D = \left[1 - \left(\frac{c_p}{c_s} \right)^2 \right] \varepsilon_{,12}^V \,,
\tag{40}
$$

where

$$
c_p = \sqrt{\frac{\lambda + 2\mu}{\rho^*}}, \qquad c_s = \sqrt{\frac{\mu}{\rho^*}}
\tag{41}
$$

are the zero-gyricity pressure and shear velocities. From (39) we note that the gyricity couples volumetric deformations and rotations, while, for $\Omega^* = 0$, the classical uncoupled homogeneous Helmholtz equations govern the wave propagation (see, for example the textbook by Graff (1975), Chapter 5.1.2).

4.1 Demonstration of the non-reciprocity of the continuous gyroscopic medium

The law of reciprocity in elastodynamics identifies a symmetry between action and reaction in solids. Reciprocity is expressed by the classical Betti's theorem (see the classical paper by Betti (1872)) in elastostatics and it was extended to elastodynamics by Graffi (1946), who implemented a convolution between two elastic states. In a simpler form, independent of initial conditions, reciprocity states that the frequency-response functions between any two material points remain the same after swapping source and receiver. Here, we demonstrate the non-reciprocity of the gyroscopic elastic system in the transient regime by considering homogeneous initial conditions and zero body forces in order to focus only on the effect of gyricity. Results can be directly extended and are valid when applied loads and non-zero initial conditions are considered.

We consider two different displacement solutions $\boldsymbol{u}^{(p)}(\mathbf{x},t)$, $p = 1,2$, where displacements $\boldsymbol{u}^{(p)}$ satisfy the transient governing equation (35). Displacements $\boldsymbol{u}^{(p)}(\mathbf{x},t)$ are associated to deformations $\hat{\boldsymbol{\varepsilon}}^{(p)}(\mathbf{x},t)$ and stresses $\hat{\boldsymbol{\sigma}}^{(p)}(\mathbf{x},t)$ by means of classical kinematic compatibility (38) and linear elastic and isotropic constitutive relations

$$
\hat{\boldsymbol{\sigma}}^{(p)}(\mathbf{x},t) = \lambda \mathrm{tr}(\hat{\boldsymbol{\varepsilon}}^{(p)}) \boldsymbol{I} + 2\mu \hat{\boldsymbol{\varepsilon}}^{(p)}, \qquad p = 1,2 \,,
\tag{42}
$$

with tr the trace operator. [*]

In order to check reciprocity, we select an arbitrary domain V, with boundary S having outward normal $\boldsymbol{n}$, and consider

$$
\mathcal{D}(\boldsymbol{u}^{(1)}, \boldsymbol{u}^{(2)}) := \int_S \left(\boldsymbol{\sigma}^{(1)} \boldsymbol{n} \right) \circ \boldsymbol{u}^{(2)} dA - \int_S \left(\boldsymbol{\sigma}^{(2)} \boldsymbol{n} \right) \circ \boldsymbol{u}^{(1)} dA \,,
\tag{43}
$$

---

[*]Note that isotropy is not an essential part with regard to reciprocity.

where $\circ$ indicates the time convolution $g \circ h = \int_0^t g(x, t - \tau) h(x, \tau) d\tau$. In what follows, where this convolution appears, we note that the product of g and h in the integrand utilises scalar or tensor products where relevant.

We deal with the first integral in (43). Note that

$$\int_S \left(\hat{\boldsymbol{\sigma}}^{(1)} \boldsymbol{n} \right) \circ \boldsymbol{u}^{(2)} dA = \int_S \left(\hat{\boldsymbol{\sigma}}^{(1)} \circ \boldsymbol{u}^{(2)} \right) \cdot \boldsymbol{n} \, dA =$$

$$\int_V \nabla \cdot \left(\hat{\boldsymbol{\sigma}}^{(1)} \circ \boldsymbol{u}^{(2)} \right) dV = \int_V (\nabla \cdot \hat{\boldsymbol{\sigma}}^{(1)}) \circ \boldsymbol{u}^{(2)} \, dV + \int_V \hat{\boldsymbol{\sigma}}^{(1)} \circ \nabla \boldsymbol{U}^{(2)} dV = \quad (44)$$

$$\int_V \left[(\lambda + \mu) \nabla (\nabla \cdot \boldsymbol{u}^{(1)}) + \mu \Delta \boldsymbol{u}^{(1)} \right] \circ \boldsymbol{u}^{(2)} dV + \int_V \hat{\boldsymbol{\sigma}}^{(1)} \circ \hat{\boldsymbol{\varepsilon}}^{(2)} dV ,$$

where we made use of the symmetry of the stress tensor in the first, third and fourth equality. Then, the second equality is a standard application of the divergence theorem. Lastly, the constitutive relation (42) and the kinematic compatibility (38) is applied to express $\nabla \cdot \hat{\boldsymbol{\sigma}}^{(1)}$ in term of the displacement field $\boldsymbol{u}^{(1)}$.

From the governing equation (35), it is evident that

$$\left[(\lambda + \mu) \nabla (\nabla \cdot \boldsymbol{u}^{(1)}) + \mu \Delta \boldsymbol{u}^{(1)} \right] \circ \boldsymbol{u}^{(2)} = \left(\rho^* \ddot{\boldsymbol{u}}^{(1)} + \rho^* \Omega^* \boldsymbol{R} \dot{\boldsymbol{u}}^{(1)} \right) \circ \boldsymbol{u}^{(2)} \quad (45)$$

and we note that, for homogeneous/zero initial conditions,

$$\ddot{\boldsymbol{u}}^{(1)} \circ \boldsymbol{u}^{(2)} = \frac{\partial^2}{\partial t^2} \left(\boldsymbol{u}^{(1)} \circ \boldsymbol{u}^{(2)} \right) = \boldsymbol{u}^{(1)} \circ \ddot{\boldsymbol{u}}^{(2)} , \quad (46)$$

and

$$\boldsymbol{R} \dot{\boldsymbol{u}}^{(1)} \circ \boldsymbol{u}^{(2)} = \frac{\partial}{\partial t} \left(\boldsymbol{R} \boldsymbol{u}^{(1)} \circ \boldsymbol{u}^{(2)} \right) = \frac{\partial}{\partial t} \left(\boldsymbol{u}^{(1)} \circ \boldsymbol{R}^T \boldsymbol{u}^{(2)} \right) =$$

$$-\frac{\partial}{\partial t} \left(\boldsymbol{u}^{(1)} \circ \boldsymbol{R} \boldsymbol{u}^{(2)} \right) = -\frac{\partial}{\partial t} \left(\boldsymbol{R} \boldsymbol{u}^{(2)} \circ \boldsymbol{u}^{(1)} \right) = -\boldsymbol{R} \dot{\boldsymbol{u}}^{(2)} \circ \boldsymbol{u}^{(1)} . \quad (47)$$

Returning back to the last integrand in (44)

$$\hat{\boldsymbol{\sigma}}^{(1)} \circ \hat{\boldsymbol{\varepsilon}}^{(2)} = \left(\lambda \text{tr}(\hat{\boldsymbol{\varepsilon}}^{(1)}) \boldsymbol{I} + 2\mu \hat{\boldsymbol{\varepsilon}}^{(1)} \right) \circ \hat{\boldsymbol{\varepsilon}}^{(2)} = \lambda \text{tr}(\hat{\boldsymbol{\varepsilon}}^{(1)}) \circ \text{tr}(\hat{\boldsymbol{\varepsilon}}^{(2)}) + 2\mu \hat{\boldsymbol{\varepsilon}}^{(1)} \circ \hat{\boldsymbol{\varepsilon}}^{(2)} =$$

$$= \left(\lambda \text{tr}(\hat{\boldsymbol{\varepsilon}}^{(2)}) \boldsymbol{I} + 2\mu \hat{\boldsymbol{\varepsilon}}^{(2)} \right) \circ \hat{\boldsymbol{\varepsilon}}^{(1)} = \hat{\boldsymbol{\sigma}}^{(2)} \circ \hat{\boldsymbol{\varepsilon}}^{(1)} = \hat{\boldsymbol{\sigma}}^{(2)} \circ \nabla \boldsymbol{u}^{(1)} ,$$
$$(48)$$

since $\boldsymbol{I} : \hat{\varepsilon}^{(p)} = \text{tr}(\hat{\boldsymbol{\varepsilon}}^{(p)})$, with $p = 1, 2$.

An analogous computation can be done for the second integral in (43) by simply commuting the indexes 1 and 2. In doing so, it is evident that analogous terms to (48) and (46) will cancel out in (43).

Therefore, the difference (43) takes the form

$$\mathcal{D}(\boldsymbol{u}^{(1)}, \boldsymbol{u}^{(2)}) = -2 \int_V \rho^* \Omega^* \boldsymbol{R} \dot{\boldsymbol{u}}^{(2)} \circ \boldsymbol{u}^{(1)} dV \quad (49)$$

which is generally non-zero. This proves that the gyroscopic medium is non-reciprocal.

14

4.2 Dispersion relation in the bulk

Now, we investigate the dispersive behaviour of the gyroscopic continuum. The solution of (37) is sought in terms of dilatational and distortional potentials $\varphi(\boldsymbol{x})$ and $\boldsymbol{\chi} = (0, 0, \chi(\boldsymbol{x}))^T$, respectively, such that the displacement $\boldsymbol{U} = \nabla\varphi + \nabla \times \boldsymbol{\chi}$. Therefore, (37) take the form

$$\nabla \left[\left((\lambda + 2\mu)\Delta + \rho^*\omega^2 \right) \varphi - \mathrm{i}\rho^*\Omega^*\omega\chi \right] + \nabla \times \left[\left(\mu\,\Delta + \rho^*\omega^2 \right) \chi + \mathrm{i}\rho^*\Omega^*\omega\varphi \right] = 0 \,, \tag{50}$$

which are satisfied by

$$\begin{aligned} \left[\Delta + \left(\frac{\omega}{c_p} \right)^2 \right] \varphi - \frac{\mathrm{i}\Omega^*\omega}{c_p^2}\chi &= 0 \,, \\ \left[\Delta + \left(\frac{\omega}{c_s} \right)^2 \right] \chi + \frac{\mathrm{i}\Omega^*\omega}{c_s^2}\varphi &= 0 \,. \end{aligned} \tag{51}$$

In a similar way to (5), we implement in (51) the solutions

$$\varphi(x_1, x_2) = D_1 \mathrm{e}^{-\eta x_2} \mathrm{e}^{\mathrm{i}k_1 x_1} \,, \quad \chi(x_1, x_2) = D_2 \mathrm{e}^{-\eta x_2} \mathrm{e}^{\mathrm{i}k_1 x_1} \,, \tag{52}$$

which lead to the homogeneous system

$$\boldsymbol{M}_3\,\boldsymbol{D} = \boldsymbol{0} \,, \tag{53}$$

where

$$\boldsymbol{M}_3 = \begin{pmatrix} \eta^2 - a_p & -\frac{\mathrm{i}\Omega^*\omega}{c_p^2} \\ \frac{\mathrm{i}\Omega^*\omega}{c_s^2} & \eta^2 - a_s \end{pmatrix} \,, \qquad \boldsymbol{D} = \begin{pmatrix} D_1 \\ D_2 \end{pmatrix} \,, \tag{54}$$

with

$$a_p = k_1^2 - \left(\frac{\omega}{c_p} \right)^2 \,, \qquad a_s = k_1^2 - \left(\frac{\omega}{c_s} \right)^2 \,. \tag{55}$$

Non-trivial solutions of (53) are obtained by setting $\det \boldsymbol{M}_3 = 0$, which yields the biquadratic equation in η:

$$\eta^4 - (a_p + a_s)\,\eta^2 + a_p a_s - \frac{(\Omega^*)^2 \omega^2}{c_s^2 c_p^2} = 0 \,, \tag{56}$$

having the four solutions

$$\eta_j = \sqrt{\frac{a_p + a_s}{2} \pm \sqrt{\frac{(\Omega^*)^2 \omega^2}{c_s^2 c_p^2} + \left(\frac{a_p - a_s}{2} \right)^2}} \,, \tag{57}$$

$$\eta_{j+2} = -\eta_j \,, \qquad\qquad j = 1, 2 \,.$$

Among the four solutions we consider the two positive ones, $\eta_1 > \eta_2 > 0$, associated with a decaying amplitude for $x_2 > 0$, which represents the considered half-plane. They are also subjected to the constraints

$$\frac{\omega}{|k_1|} \le \left[\frac{1}{2} \left(\frac{1}{c_s^2} + \frac{1}{c_p^2} \right) \pm \sqrt{\frac{(\Omega^*)^2}{\omega^2 c_s^2 c_p^2} + \frac{1}{4} \left(\frac{1}{c_s^2} - \frac{1}{c_p^2} \right)^2} \right]^{-\frac{1}{2}} \,. \tag{58}$$

15

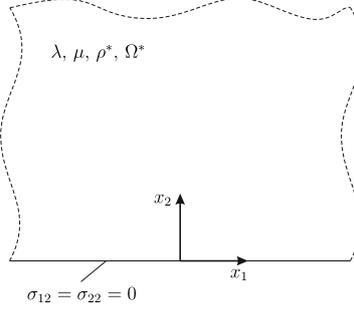Figure 5: Semi-infinite gyroscopic continuum, characterised by Lamé moduli λ and μ, effective density ρ^* and effective gyricity Ω^*, having a traction-free boundary at $x_2 = 0$.

The associated eigenvectors are $\boldsymbol{A}^{(1)} = (1, A^{(1)})^{\mathrm{T}}$ and $\boldsymbol{A}^{(2)} = (1, A^{(2)})^{\mathrm{T}}$, where

$$A^{(1)} = \mathrm{i}\,\dfrac{\dfrac{a_p - a_s}{2} - \sqrt{\dfrac{(\Omega^*)^2 \omega^2}{c_p^2 c_s^2} + \left(\dfrac{a_p - a_s}{2}\right)^2}}{\dfrac{\Omega^* \omega}{c_p}} \tag{59a}$$

and

$$A^{(2)} = \mathrm{i}\,\dfrac{\dfrac{a_p - a_s}{2} + \sqrt{\dfrac{(\Omega^*)^2 \omega^2}{c_p^2 c_s^2} + \left(\dfrac{a_p - a_s}{2}\right)^2}}{\dfrac{\Omega^* \omega}{c_p}} \,. \tag{59b}$$

In passing, we also note that plane waves in the bulk can be obtained by setting $\eta = -ik_2$. In such a case, the dispersion relation (56) has the explicit solutions

$$\omega_{1,2} = \sqrt{\frac{c_p^2 + c_s^2}{2} k^2 + \frac{(\Omega^*)^2}{2} \pm \frac{1}{2}\sqrt{\left(c_p^2 - c_s^2\right)^2 k^4 + 2(c_p^2 + c_s^2)\,(\Omega^*)^2\,k^2 + (\Omega^*)^4}}\,, \tag{60}$$

with $k = \sqrt{k_1^2 + k_2^2}$. For $\Omega^* = 0$, expressions (60) reduce to the classical zero-gyricity solutions

$$\omega_1 = c_p k = \sqrt{\frac{\lambda + 2\mu}{\rho^*}}\,k, \qquad \omega_2 = c_s k = \sqrt{\frac{\mu}{\rho^*}}\,k\,. \tag{61}$$

4.3 Surface waves in the semi-infinite continuous medium

In the semi-infinite continuous medium $(x_1, x_2) \in \mathbb{R}_+^2 = \{(x_1, x_2) : x_1 \in \mathbb{R}, x_2 \geq 0\}$ (see Fig. 5), free-boundary conditions are applied at $x_2 = 0$. They are expressed in terms of Cauchy stress components

$$\sigma_{12}(x_1, 0) = \mu(U_{1,2} + U_{2,1}) = \mu(2\varphi_{,12} + \chi_{,22} - \chi_{,11}) = 0\,,$$
$$\sigma_{22}(x_1, 0) = \lambda U_{1,1} + (\lambda + 2\mu)U_{2,2} = (\lambda + 2\mu)\Delta\varphi - 2\mu(\varphi_{,1} + \chi_{,2})_{,1} = 0\,. \tag{62}$$

The dilatational and distortional potentials admit the representations

$$\varphi(x_1, x_2) = \left(E_1 \mathrm{e}^{-\eta_1 x_2} + E_2 \mathrm{e}^{-\eta_2 x_2}\right) \mathrm{e}^{\mathrm{i}k_1 x_1}\,,$$
$$\chi(x_1, x_2) = \left(E_1 A^{(1)} \mathrm{e}^{-\eta_1 x_2} + E_2 A^{(2)} \mathrm{e}^{-\eta_2 x_2}\right) \mathrm{e}^{\mathrm{i}k_1 x_1}\,, \tag{63}$$

16

which can be implemented into the boundary conditions (62) to give, after algebraic manipulations, the homogeneous system

$$\boldsymbol{M}_4 \, \boldsymbol{E} = \boldsymbol{0} \,, \tag{64}$$

where

$$\boldsymbol{M}_4 = \begin{pmatrix} (\eta_1^2 + k_1^2)A^{(1)} - 2\mathrm{i}k_1\eta_1 & (\eta_2^2 + k_1^2)A^{(2)} - 2\mathrm{i}k_1\eta_2 \\ \dfrac{(1-\nu)\eta_1^2 - \nu k_1^2}{1 - 2\nu} + \mathrm{i}k_1\eta_1 A^{(1)} & \dfrac{(1-\nu)\eta_2^2 - \nu k_1^2}{1 - 2\nu} + \mathrm{i}k_1\eta_2 A^{(2)} \end{pmatrix} \tag{65}$$

and $\boldsymbol{E} = (E_1, E_2)^{\mathrm{T}}$. Then, non-trivial solutions of the system (64) are obtained by setting $\det \boldsymbol{M}_4 = 0$, which yields the dispersion equation for Rayleigh waves, that has the form

$$4\sqrt{\beta}\left[\frac{1-\nu}{1-2\nu}\left(\frac{\omega}{c_p}\right)^2\left(\frac{\omega^2 - (\Omega^*)^2}{2c_s^2} - k_1^2\right) + \left(k_1^2 - \eta_1\eta_2 - \frac{1}{2}\left(\frac{\omega}{c_s}\right)^2\right)k_1^2\right]$$

$$- k_1\frac{\Omega^*\omega}{c_p^2}\left[2\frac{1-\nu}{1-2\nu}\left(\tau(\eta_1-\eta_2) + \sqrt{\beta}(\eta_1+\eta_2)\right) - 2k_1^2(\eta_1-\eta_2)\right. \tag{66}$$

$$\left. + \left(\frac{c_p}{c_s}\right)^2\left((\tau - 2k_1^2)(\eta_1 - \eta_2) + \sqrt{\beta}(\eta_1 + \eta_2)\right)\right] = 0 \,,$$

where

$$\beta = \frac{(\Omega^*)^2\omega^2}{c_p^2 c_s^2} + \left(\frac{a_p - a_s}{2}\right)^2 \quad \text{and} \quad \tau = k_1^2 - \frac{a_p + a_s}{2} \,. \tag{67}$$

Interestingly, for the continuous analogue of the triangular lattice ($\nu = 0.25$), it is possible to find the following explicit solution:

$$\omega_{\mathrm{R}}^C = \sqrt{\frac{12\,c_s^2\,k_1^2 + 3(\Omega^*)^2 - \sqrt{48\,c_s^4\,k_1^4 + 72\,c_s^2\,k_1^2\,(\Omega^*)^2 + 9(\Omega^*)^4}}{6}} \,. \tag{68}$$

Note also that, when $\Omega^* = 0$, (66) reduces to the well-known dispersion relation governing Rayleigh waves in a non-gyroscopic linear elastic isotropic continuum (see, for example the book of Graff (1975), (6.1.86))

$$\left(2 - \left(\frac{c}{c_s}\right)^2\right)^2 = 4\sqrt{1 - \left(\frac{c}{c_p}\right)^2}\sqrt{1 - \left(\frac{c}{c_s}\right)^2}\,, \qquad c = \frac{\omega}{k_1} \,, \tag{69}$$

which, for a Poisson's ratio $\nu = 0.25$, has the explicit form

$$\frac{c}{c_s} = \sqrt{\frac{2}{3}}\sqrt{3 - \sqrt{3}} \simeq 0.919402 \,. \tag{70}$$

For the interested reader, the solutions of (69) for any value of the Poisson's ratio are reported in Appendix A.

The Rayleigh dispersion curve ω_{R}^C in (68), together with the dispersion curves ω_1 and ω_2 in (60) for bulk waves, indicate a dispersive behaviour. We note that $\omega_2 < \omega_1$ and $\omega_R^C < \omega_2$ for all $k_1 \neq 0$, as in the classical case for $\Omega^* = 0$. In addition, the upper dispersion curve ω_1 has the lower cut-off frequency $\omega = \Omega^*$.

Furthermore, dispersion curves remain symmetric in k_1, as also evidenced in (68). Thus, it is important to stress that non-reciprocity cannot be attributed to a lack of symmetry of the dispersion curves, but to the non-symmetric eigenmodes, as shown in Figure 4.

It is also of interest to analyse the dispersive behaviour when the gyricity is linked to the radian frequency, as studied by Brun et al. (2012), Carta et al. (2014), namely $\Omega^* = \alpha\,\omega$ (a restrictive assumption that was removed in the works of Carta et al. (2018), Nieves et al. (2018), Garau et al. (2019)). In such a case, by repeating the analysis developed in Sections 4.2 and 4.3, it has been checked that the dispersion curves for Rayleigh waves maintain the symmetry with respect to k_1, independently of the value of the coupling parameter α. In particular, for the continuous analogous of the lattice, the explicit solution can be found by solving eq. (68), with $\Omega^* = \alpha\,\omega$. Such solution, valid for every $\alpha \in \mathbb{R}$, is

$$\omega_R^C = c_s\sqrt{\frac{2}{3}}\sqrt{\frac{3 - \sqrt{3 + 6\alpha^2}}{1 - \alpha^2}}|k_1|. \tag{71}$$

These analytical results are in contrast with the numerical findings of Zhao et al. (2020)[†] (see, in particular, Fig. 7 and the discussion in Section 4.3 presented there), as (71) shows the dispersion curves are symmetric about the zero wavenumber, while in Zhao et al. (2020) they are not. We emphasise that the non reciprocal effect cannot be attributed to a lack of symmetry of the dispersion curves.

4.4 Discrete vs Continuum

In Fig. 6 the results for the lattice and the continuum approximation are compared. The results are given following the normalisation (6), with

$$c_{s,p} = \tilde{c}_{s,p}\sqrt{\frac{\gamma L^2}{m^*}} \quad \text{and} \quad \tilde{c}_s = \frac{\tilde{c}_p}{\sqrt{3}} = \sqrt{\frac{3}{8}}. \tag{72}$$

In particular, when $k_1 \to 0$,

$$
\begin{aligned}
\omega_{\mathrm{R}}^C &= \frac{\sqrt{3 - \sqrt{3}}}{2}k_1\,, & &\text{when} \quad \Omega^* = 0\,, \\
\omega_{\mathrm{R}}^C &\sim \frac{\sqrt{3}}{2\sqrt{2}\Omega^*}k_1^2 - \frac{3\sqrt{3}}{8(\Omega^*)^3}k_1^4 + O(k_1^6)\,, & &\text{when} \quad \Omega^* \neq 0\,.
\end{aligned}
\tag{73}
$$

Such results confirm that the dispersive behaviour of the gyroscopic medium is parabolic for $k_1 \to 0$, as in the case of flexural waves in Euler-Bernoulli beams or Kirchhoff plates. The comparative analysis between the asymptotic results in (26) and (73) shows that the continuum approximation is exact up to second order in k_1.

4.5 Eigenvectors and trajectories of the particles on the surface of the gyroscopic continuum

Considering the continuum approximation of the triangular lattice ($\nu = 0.25$), the displacement amplitudes on the surface $x_2 = 0$ are given by (see (65) and

---

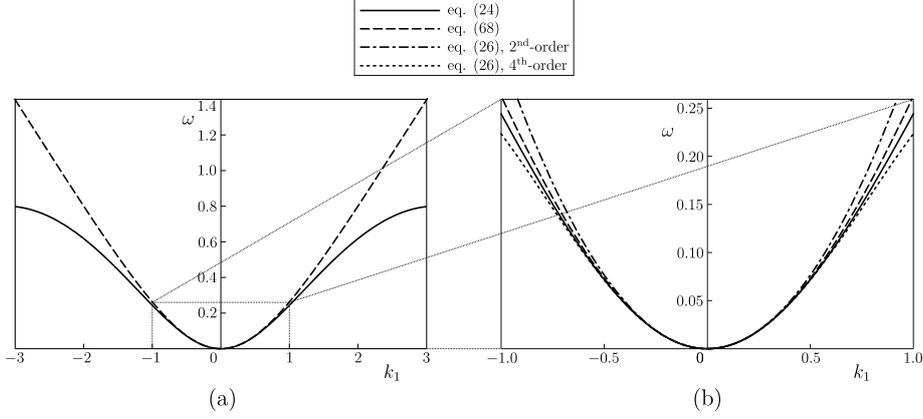[†]The parameter α in (71) corresponds to α/ρ in Zhao et al. (2020).

Figure 6: Dispersion curves for Rayleigh waves in a gyroscopic medium. Plain and dashed lines correspond, respectively, to the triangular lattice (eq. (24)) and to the continuous approximation (eq. (68)), respectively. In part (b) a magnification of part (a) in the range $k_1 \in [-1, 1]$ is presented. The additional dot-dashed and dotted lines correspond to the second- and fourth-order approximations of the dispersion curve of the lattice (eq. (26)), respectively. The curves are obtained for an effective gyricity $\Omega^* = 2$.

(59))

$$
\begin{aligned}
U_1 &= \left[(\mathrm{i}k_1 - \eta_1 A^{(1)})E_1 + (\mathrm{i}k_1 - \eta_2 A^{(2)})E_2 \right] \mathrm{e}^{\mathrm{i}k_1 x_1} , \\
U_2 &= - \left[(\eta_1 + \mathrm{i}k_1 A^{(1)})E_1 + (\eta_2 + \mathrm{i}k_1 A^{(2)})E_2 \right] \mathrm{e}^{\mathrm{i}k_1 x_1} .
\end{aligned}
\tag{74}
$$

Referring to the equation (30) of an ellipse, since $U_2 = (|U_2|/|U_1|)U_1 \mathrm{e}^{\pm \mathrm{i}\pi/2}$, it turns out that the trajectory of any particle on the free surface is an ellipse, with principal axes aligned with x_1 and x_2 and having lengths equal to $|U_1|$ and $|U_2|$, respectively.

When $\Omega^* = 0$

$$
\begin{aligned}
U_1 &= \frac{\sqrt{3} - 1}{\sqrt{3}} \mathrm{i}k_1 E_1 \mathrm{e}^{\mathrm{i}k_1 x_1} , \\
U_2 &= \sqrt{\frac{2\sqrt{3} + 3}{3}} \frac{\sqrt{3} - 1}{\sqrt{3}} |k_1| E_1 \mathrm{e}^{\mathrm{i}k_1 x_1} .
\end{aligned}
\tag{75}
$$

As in the discrete case, the trajectory is an ellipse with principal axes aligned with x_1 and x_2. The ratio between the lengths of the semi-axes is given by

$$
\frac{|U_1|}{|U_2|} = \sqrt{\frac{3}{2\sqrt{3} + 3}} = 0.68125 .
\tag{76}
$$

The ratio between the lengths of the semi-axes along x_1 and x_2, denoted as ξ_1/ξ_2 as in Section 3.2, is shown in Fig. 7(a) for the same values of Ω^* considered in Fig. 4. We note that in the limit when $k_1 \to 0$, the values of the ratio ξ_1/ξ_2, for both $\Omega^* = 0$ and $\Omega^* \neq 0$, coincide with those obtained for the triangular lattice, reported in Fig. 4 (see comparison in Fig. 7(b)). The same lack of symmetry around $k_1 = 0$ is retrieved, with oscillations only along x_2 for $k_1 \to 0^-$.
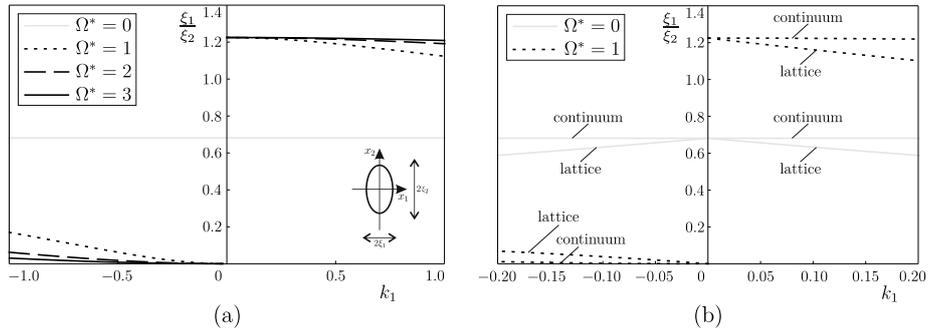
Figure 7: (a) Ratio between the lengths of the semi-axes of the elliptical trajectories of the particles on the free surface of the gyroscopic continuum, calculated for different values of the effective gyricity Ω^*; (b) comparison of the ratios ξ_1/ξ_2 in the lattice and in the continuum, evaluated for $\Omega^* = 0$ and $\Omega^* = 1$.

5 Response of the lattice half-plane to a time-harmonic force applied on the boundary

In this section, we study the dynamic behaviour of the gyro-elastic lattice subjected to a time-harmonic loading imposed on the boundary. We will show that the main effect of the gyricity is to break the symmetry of the lattice response and create preferential directionality in the energy radiated from the external source.

We recall that Fig. 3 is useful to describe the propagation of Rayleigh waves supported along the lattice boundary in the time-harmonic regime. It is also valuable in studying the time-harmonic response of the lattice when the boundary is loaded. In this case, the dispersive analysis of Rayleigh waves is associated with the behaviour of the boundary when observed at a sufficiently large distance from the load. In particular, Fig. 3 can be used to specify the direction in which Rayleigh waves propagate relative to the load. This follows as a direct consequence of the causality principle (see the book of [Slepyan (2001)], Sections 3.3.2 and 3.3.3), which may be employed to show that waves propagating to the right of the load have positive group velocity, while waves propagating to the left have negative group velocity. Hence, comparing Fig. 3 with Fig. 4, we deduce that the elliptical trajectories corresponding to positive (negative) wavenumbers are observed to the right (left) of the force, where the size of the trajectory is scaled by the forcing amplitude. Additionally, for positive gyricity, the trajectories in Fig. 4 for wavenumbers with the same magnitude but opposite sign are different. Accordingly, we expect non-symmetric lattice response along the boundary sufficiently far from the load.

5.1 Governing equations of the forced lattice

In the bulk of the medium, the governing equations for the displacements of the lattice particles are still given by (7). Conversely, for the nodes along the

20

boundary, the equations of motion (16) become:

$$
\begin{aligned}
-\omega^2 \boldsymbol{U}^{(n_1,0)} = \mathrm{i}\omega\,\Omega^* \boldsymbol{R}\boldsymbol{U}^{(n_1,0)} &+ \Big[\boldsymbol{a}^{(1)} \cdot \Big(\boldsymbol{U}^{(n_1+1,0)} + \boldsymbol{U}^{(n_1-1,0)} - 2\boldsymbol{U}^{(n_1,0)} \Big) \boldsymbol{a}^{(1)} \\
&+ \boldsymbol{a}^{(2)} \cdot \Big(\boldsymbol{U}^{(n_1,1)} - \boldsymbol{U}^{(n_1,0)} \Big) \boldsymbol{a}^{(2)} + \boldsymbol{a}^{(3)} \cdot \Big(\boldsymbol{U}^{(n_1-1,1)} - \boldsymbol{U}^{(n_1,0)} \Big) \boldsymbol{a}^{(3)} \Big] \\
&+ \boldsymbol{P}\delta^{(n_1,0)}\,, \qquad n_1 \in \mathbb{Z}\,,
\end{aligned}
\tag{77}
$$

where the force has (normalised) amplitude vector $\boldsymbol{P}$. According to the normalisation introduced in Section 2.1, the dimensional amplitude vector of the force is given by $\gamma L \boldsymbol{P}$. We also recall that $\Omega^* = \alpha\Omega$ is the effective gyricity and $\delta^{(i,j)} = \delta_{ij}$ denotes the Kronecker delta.

The forced problem defined by (7) and (77) is solved with a finite element code developed in *Comsol Multiphysics* (version 5.4). The results of the numerical simulations are presented in the next Section.

5.2 Effect of gyricity on the displacement field in the lattice

Figure 8 shows the total displacement amplitude in each node of the elastic lattice. In parts (a) and (b) the effective gyricity is zero, while in parts (c) and (d) $\Omega^* = 1$. The external force is applied on the boundary and acts in the horizontal (vertical) direction in parts (a) and (c) (parts (b) and (d)). In each of the four cases considered, the force has unit amplitude and radian frequency $\omega_0 = 0.8$. "Adaptive Absorbing Layers" (AAL) are introduced into the model. They consist of links with complex elastic modulus, which damp the amplitudes of waves propagating to the limits of the domain and prevent reflection of waves at the boundaries.

Comparing parts (a) and (b) with parts (c) and (d) in Fig. 8, it is apparent that gyricity breaks the symmetry in the response of the medium to the external loading. The non-symmetry of the total displacement amplitude field with respect to the vertical line passing through the point of application of the force is more evident when the force acts in the horizontal direction (see part (c)). A quantitative estimate of this observation will be addressed in Section 5.3 by calculating the energy flow.

The results of Fig. 8 show that the external excitation produces both Rayleigh waves, travelling along the surface of the medium, and waves propagating into the bulk, the amplitudes of which are larger in correspondence of specific rays emanating from the external source, located at $60°$ and $120°$ to the positive horizontal axis. We also note that in part (a) (part (b)) the waves are mainly of shear (pressure) type. When gyricity is introduced into the system, the wavelength is decreased, since for the same frequency the wavenumber is larger when $\Omega^* = 1$ with respect of the case when the effective gyricity is zero (see the dispersion diagram in Fig. 3).

Similar considerations can be made for Fig. 1 in the Introduction. In that case, the radian frequency of the external force is taken as $\omega = 0.4$. A thorough parametric analysis involving the main parameters of the system will be carried out in a future investigation.
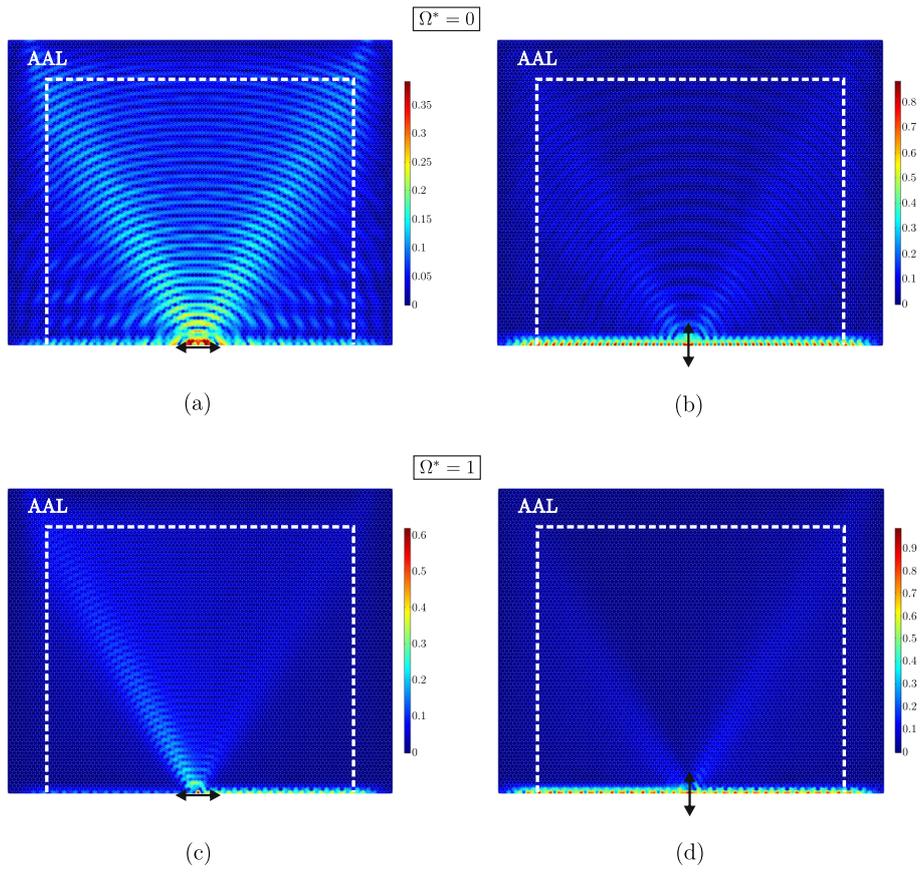
Figure 8: Total displacement amplitude field in the elastic lattice with (a,b) $\Omega^* = 0$, (c,d) $\Omega^* = 1$. The direction of the applied force is shown by an arrow in each figure. The dashed lines indicate the internal boundary of the region with "Adaptive Absorbing Layers" (AAL).
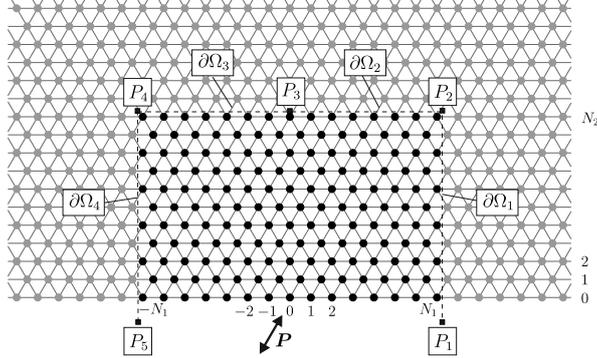
Figure 9: Region of the micro-structured medium where the energy flow is computed.

5.3 Evaluation of energy flow

Here, we calculate the energy flow associated with the Rayleigh waves, propagating along the half-plane boundary of the medium, and with the waves radiated into the bulk. In particular, we compute the energy balance in a finite region of the elastic lattice, represented by the rectangle delimited by dashed lines in Fig. 9. This rectangle is enclosed by the half-plane boundary and by the internal boundary $\partial\Omega = \cup_{i=1}^{4}\partial\Omega_i$, where each segment $\partial\Omega_i$ connects the points P_i and P_{i+1} $(i = 1, ..., 4)$.

The time-harmonic force $\boldsymbol{P}$ applied at the node $(n_1, n_2) = (0, 0)$ furnishes the system with the energy rate

$$W^{(\text{in})} = \frac{1}{2}Re[\boldsymbol{P} \cdot \bar{\boldsymbol{v}}^{(0,0)}]\,, \tag{78}$$

where $\bar{\boldsymbol{v}}^{(\boldsymbol{n})}$ is the complex conjugate of the velocity $\boldsymbol{v}^{(\boldsymbol{n})} = \dot{\boldsymbol{u}}^{(\boldsymbol{n})}$ and Re the real part. The energy flux rate through each segment $\partial\Omega_i$ $(i = 1, ..., 4)$ is calculated by means of the classical formula (see the book of Brillouin (1953), Chap. V):

$$W_i^{(\text{out})} = -\frac{1}{2}\sum_{\boldsymbol{n}_j \in D_i} Re[\boldsymbol{F}^{(\boldsymbol{n}_j)} \cdot \bar{\boldsymbol{v}}^{(\boldsymbol{n}_j)}]\,, \tag{79}$$

where $\boldsymbol{F}^{(\boldsymbol{n}_j)}$ is the total elastic force provided by the nodes outside the considered region and connected to the node denoted by $\boldsymbol{n}_j$ by links that cross the boundary $\partial\Omega_i$. The set of nodes $\boldsymbol{n}_j$ positioned in the proximity of $\partial\Omega_i$ is indicated by D_i in (79). The conservation of energy law imposes that

$$W^{\text{in}} = \sum_{i=1}^{4} W_i^{\text{out}}\,. \tag{80}$$

For the same amplitude and frequency of the external force, the amount of energy flowing through each of the four segments $\partial\Omega_i$ strongly depends on the gyricity and the direction of the force. In Fig. 10 we report the numerical outcomes obtained from the model built in *Comsol Multiphysics* for two values of effective gyricity ($\Omega^* = 0$ and $\Omega^* = 1$) and for horizontally- and vertically-acting loads. From (79), $W_i^{(\text{out})}$ is the energy flow across the segment $\partial\Omega_i$ $(i = 1, ..., 4)$.
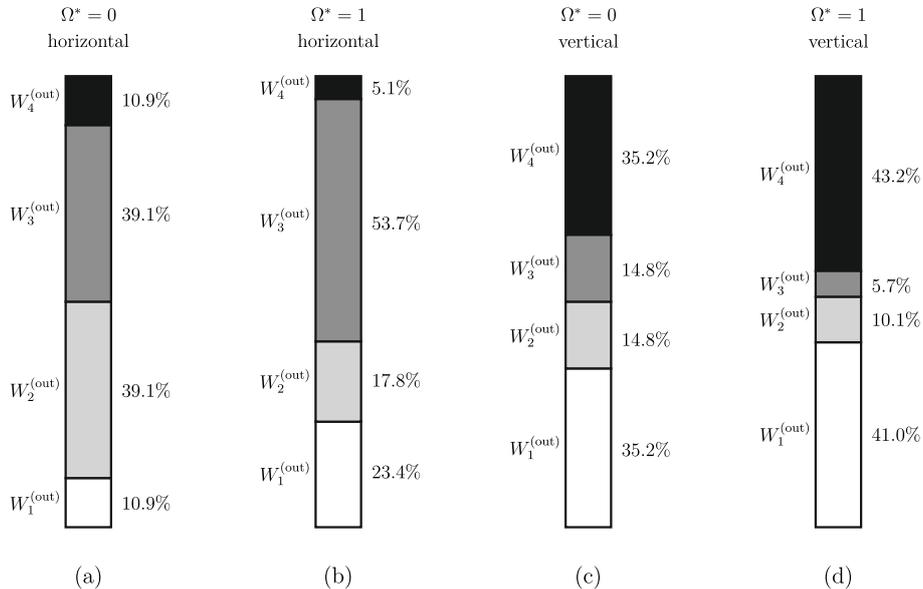
23

Figure 10: Energy flow percentages calculated for an effective gyricity (a,c) $\Omega^* = 0$ and (b,d) $\Omega^* = 1$, due to a force acting in the (a,b) horizontal and (c,d) vertical direction.

When the effective gyricity is zero, the total displacement field is symmetric with respect to a vertical line passing through the point of application of the force, namely $W_1^{(\text{out})} = W_4^{(\text{out})}$ and $W_2^{(\text{out})} = W_3^{(\text{out})}$. Of course, the distribution of energy between vertical and horizontal boundaries depends on the direction of the force. Conversely, for a non-zero value of the effective gyricity, the symmetry in the energy flow is broken. In particular, we notice a clear disparity in the symmetry for case (b), where the force acts in the horizontal direction.

The results presented in this section demonstrate that gyroscopic spinners can be exploited to create energy splitters, namely systems that force the energy coming from an external source to propagate non-symmetrically along preferential directions.

5.4   Non-reciprocity in the gyroscopic lattice

The introduction of gyroscopic spinners into the lattice breaks reciprocity of the system. In order to better illustrate this statement, we present here the results of numerical simulations performed in the transient regime.

The lattice is subjected to a force, applied at node A (or B) on the boundary, denoted as $\boldsymbol{P}^{\text{A}}$ (or $\boldsymbol{P}^{\text{B}}$) (see Fig. 11(a)). The magnitude of the force is a function of time and is taken as $P_0 \sin(\omega_0 t)$, where $P_0 = 1$ and $\omega_0 = 0.8$, as in Fig. 8. The time-history of the displacement $\boldsymbol{u}^{\text{BA}}$ (or $\boldsymbol{u}^{\text{AB}}$) at node B (or A) is shown in Fig. 11(b) and 11(c) when the force acts in the x_1- and x_2-direction, respectively. In all the diagrams, the green (or blue) line represents the magnitude of the displacement in B (or A) due to a force in A (or B), given by $\sqrt{\left(u_1^{\text{BA}}\right)^2 + \left(u_2^{\text{BA}}\right)^2}$ (or $\sqrt{\left(u_1^{\text{AB}}\right)^2 + \left(u_2^{\text{AB}}\right)^2}$). For both directions of the force, the outcomes are given when the effective gyricity is $\Omega^* = 0$ (diagrams on the
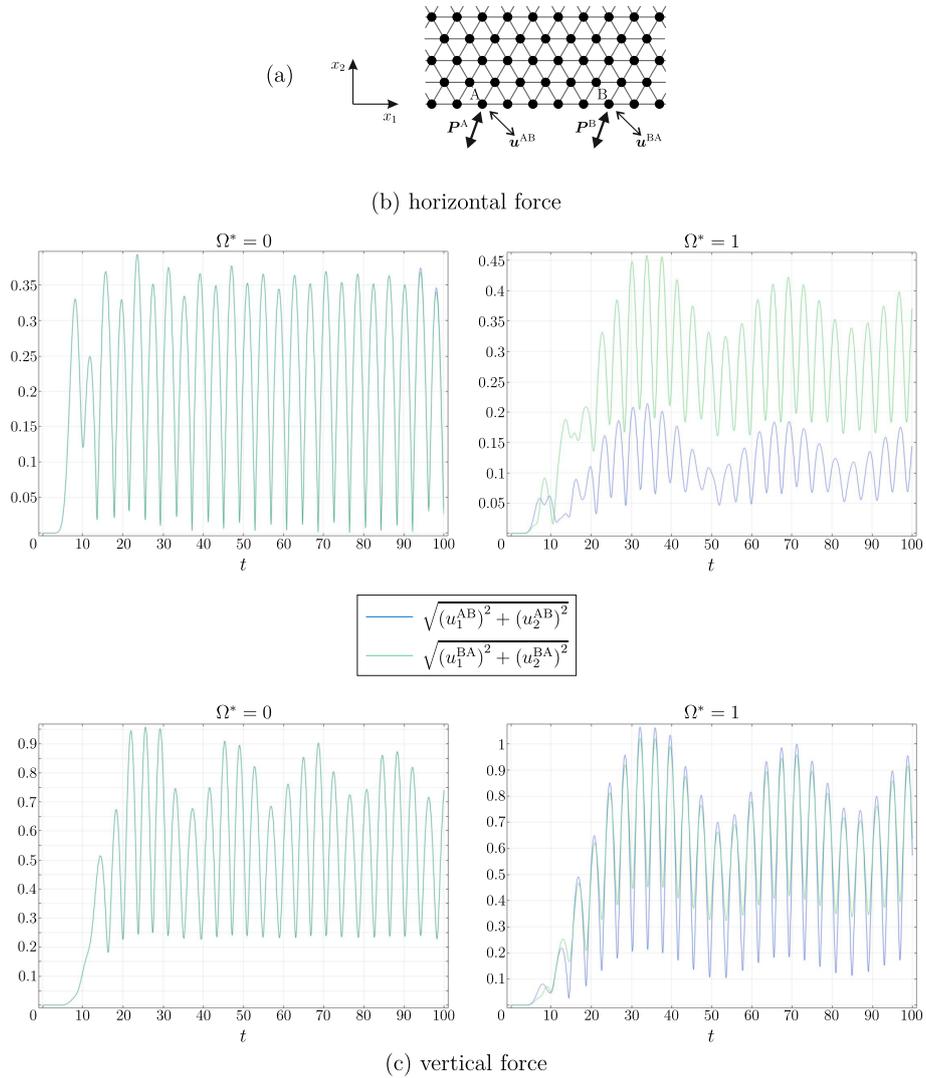
Figure 11: Numerical illustration of the non-reciprocity in the gyroscopic lattice: (a) concentrated forces and calculated displacements at the boundary; (b) time-histories of the displacements $\boldsymbol{u}^{\mathrm{BA}}$ (due to $\boldsymbol{P}^{\mathrm{A}}$) and $\boldsymbol{u}^{\mathrm{AB}}$ (due to $\boldsymbol{P}^{\mathrm{B}}$) when $\Omega^* = 0$ (left) and $\Omega^* = 1$ (right), for a force acting in the horizontal direction; (c) same as in (b), but for a vertically-acting force.

left) and $\Omega^* = 1$ (diagrams on the right).

From the diagrams on the left of Figs. 11(b) and 11(c), it is apparent that when the effective gyricity is zero the system is reciprocal. On the other hand, the diagrams on the right of Figs. 11(b) and 11(c) show that in the presence of gyroscopic spinners the two displacements are different, hence the system is non-reciprocal.

The complex amplitudes of the horizontal and vertical components of the displacements $\boldsymbol{u}^{\mathrm{BA}}$ and $\boldsymbol{u}^{\mathrm{AB}}$, calculated in the time-harmonic regime for the cases of horizontally- and vertically-acting force, are also reported in Tables 1

Table 1: Amplitudes of the displacement components of points A and B in Fig. 11(a), computed in the time-harmonic regime and due to a force of unit amplitude and frequency $\omega_0 = 0.8$ acting in the x_1-direction, for two different values of the effective gyricity Ω^*.

		$\Omega^* = 0$	$\Omega^* = 1$
point B	u_1^{BA}	$0.198 + 0.180\,\mathrm{i}$	$0.032 - 0.015\,\mathrm{i}$
	u_2^{BA}	$0.209 + 0.035\,\mathrm{i}$	$0.140 + 0.098\,\mathrm{i}$
point A	u_1^{AB}	$0.200 + 0.171\,\mathrm{i}$	$0.129 - 0.140\,\mathrm{i}$
	u_2^{AB}	$-0.220 - 0.034\,\mathrm{i}$	$0.295 + 0.245\,\mathrm{i}$

Table 2: Same as in Table 1, but for a force acting in the x_2-direction.

		$\Omega^* = 0$	$\Omega^* = 1$
point B	u_1^{BA}	$-0.221 - 0.034\,\mathrm{i}$	$-0.141 - 0.097\,\mathrm{i}$
	u_2^{BA}	$0.048 + 0.813\,\mathrm{i}$	$0.581 - 0.663\,\mathrm{i}$
point A	u_1^{AB}	$0.217 + 0.034\,\mathrm{i}$	$-0.294 - 0.245\,\mathrm{i}$
	u_2^{AB}	$0.046 + 0.810\,\mathrm{i}$	$0.547 - 0.626\,\mathrm{i}$

and 2. The data in Tables 1 and 2 are in full agreement with the results in Fig. 11. Neglecting small numerical errors, it can be noticed that reciprocity is retrieved when the effective gyricity is zero. The differences in sign indicate different rotations between the particles to the left and to the right of the force, as expected. On the other hand, the system exhibits a non-reciprocal behaviour if gyroscopic spinners are attached to the lattice, since the amplitudes of the displacements of points A and B are clearly very different when $\Omega^* = 1$.

6   Conclusions

In this contribution, we have studied the propagation of Rayleigh waves in an elastic lattice connected to a system of gyroscopic spinners. Firstly, we have derived a closed-form expression for the dispersion relation associated with surface waves, which shows that the width of the pass-band of the system decreases as the gyricity of the spinners is increased. Further, the study of the eigenmodes has revealed that the shape of the elliptical trajectories of the lattice particles is different for wavenumbers having the same magnitude but opposite sign.

Successively, the non-symmetry of the eigenvectors is investigated more comprehensively by solving a forced problem, where the lattice is excited by a point force on the boundary. When gyricity is introduced into the model, the total displacement field is not symmetric with respect to a line perpendicular to the

boundary and passing through the point of application of the force. Quantitative considerations on the energy flow through the boundaries of a region inside the system have also shown that the preferential directionality of energy propagation depends on the direction of the force as well as on the gyricity of the spinners and the frequency of the external force.

Furthermore, a continuum approximation of the gyroscopic discrete medium has been proposed. As for the lattice, a thorough dispersion analysis has been performed, which has led to a closed-form dispersion equation. Moreover, even in the continuum case it has been found that the elliptical trajectories of the points of the medium are not symmetric with respect to the vertical axis of the dispersion diagram. Asymptotic estimates of the dispersion relations have shown that the continuum approximation is exact up to the second order in the wavenumber. A formal demonstration of the non-reciprocity property is given for the continuum case. It has also been shown that non-reciprocity results from the asymmetry of the internal eigenmodes, but not on the dispersion curves which remain symmetric.

The gyroscopic system studied in this paper can have important applications in many fields of engineering. In particular, the possibility of breaking the symmetry of energy propagation can be exploited to design special devices that divert the energy coming from an external source to prescribed directions on the boundary or in the bulk of a system.

References

Abouelregal AE. (2011). Rayleigh waves in a thermoelastic solid half space using dual-phase-lag model. *Int. J. Eng. Sci.* **49**, 781-791.

Achenbach JD. (1973). *Wave Propagation in Elastic Solids*. North-Holland Series in Applied Mathematics and Mechanics Vol. 16., North-Holland Publishing Company, Amsterdam, London.

Akbarov SD, Ozisik M. (2003). The influence of the third order elastic constants to the generalized Rayleigh wave dispersion in a pre-stressed stratified half-plane. *Int. J. Eng. Sci.* **41**, 2047–2061.

Antonakakis T, Craster RV, Guenneau S, Skelton EA. (2014). An asymptotic theory for waves guided by diffraction gratings or along microstructured surfaces. *Proc. R. Soc. A* **470**, 20130467.

Ayzenberg-Stepanenko M, Mishuris G, Slepyan L. (2014). Brittle fracture in a periodic structure with internal potential energy. Spontaneous crack propagation. *Proc. R. Soc. A* **470**, 20140121.

Betti E. (1872). *Il Nuovo Cimento*. Series 2, Vol. 7-8.

Brillouin L. (1953). *Wave propagation in periodic structures. Electric filters and crystal lattices.* Second edition, Dover Publications, Inc..

Brun M, Jones IS, Movchan AB. (2012). Vortex-type elastic structured media and dynamic shielding. *Proc. R. Soc. A* **468**, 3027–3046.

Carta G, Brun M, Movchan AB, Movchan NV, Jones IS. (2014). Dispersion properties of vortex-type monatomic lattices. *Int. J. Solids Struct.* **51**, 2213–2225.

Carta G, Jones IS, Movchan NV, Movchan AB, Nieves MJ. (2017). "Deflecting elastic prism" and unidirectional localisation for waves in chiral elastic systems. *Sci. Rep.* **7**, 26.

Carta G, Nieves MJ, Jones IS, Movchan NV, Movchan AB. (2018). Elastic chiral waveguides with gyro-hinges. *Quart. J. Mech. Appl. Math.* **71**, 157–185.

Carta G, Colquitt DJ, Movchan AB, Movchan NV, Jones IS. (2019). One-way interfacial waves in a flexural plate with chiral double resonators. *Phil. Trans. R. Soc. A* **378**, 20190350.

Carta G, Jones IS, Movchan NV, Movchan AB. (2019). Wave polarization and dynamic degeneracy in a chiral elastic lattice. *Proc. R. Soc. A* **475**, 20190313.

Carta G, Colquitt DJ, Movchan AB, Movchan NV, Jones IS. (2020). Chiral flexural waves in structured plates: Directional localisation and control. *J. Mech. Phys. Solids* **137**, 103866.

Chandrasekharaiah DS. (1987). Effects of surface stresses and voids on Rayleigh waves in an elastic solid. *Int. J. Eng. Sci.* **25**, 205–211.

Chiri S, Ghiba ID. (2012). Rayleigh waves in Cosserat elastic materials. *Int. J. Eng. Sci.* **51**, 117–127.

Colquitt DJ, Craster RV, Antonakakis T, Guenneau S. (2015). Rayleigh-Bloch waves along elastic diffraction gratings. *Proc. R. Soc. A* **471**, 20140465.

Colquitt DJ, Colombi A, Craster RV, Roux P, Guenneau S. (2017). Seismic metasurfaces: Sub-wavelength resonators and Rayleigh wave interaction. *J. Mech. Phys. Solids* **99**, 379–393.

Colombi A, Colquitt DJ, Roux P, Guenneau S, Craster RV. (2016). A seismic metamaterial: the resonant metawedge. *Sci. Rep.* **6**, 27717.

Del Vescovo D, Giorgio I. (2014). Dynamic problems for metamaterials: Review of existing models and ideas for further research. *Int. J. Eng. Sci.* **80**, 153–172.

Evans DV, Porter R. (2008). Flexural waves on a pinned semi-infinite thin elastic plate. *Wave Motion* **45**(6), 745–757.

Fu Y, Kaplunov J, Prikazchikov D. (2020). Reduced model for the surface dynamics of a generally anisotropic elastic half-space. *Proc. R. Soc. A* **476**, 20190590.

Garau M, Carta G, Nieves MJ, Jones IS, Movchan NV, Movchan AB. (2018). Interfacial waveforms in chiral lattices with gyroscopic spinners. *Proc. R. Soc. A.* **474**, 20180132.

Garau M, Nieves MJ, Carta G, Brun M. (2019). Transient response of a gyroelastic structured medium: Unidirectional waveforms and cloaking. *Int. J. Eng. Sci.* **143**, 115–141.

Georgiadis HG, Velgaki EG. (2003). High-frequency Rayleigh waves in materials with micro-structure and couple-stress effects. *Int. J. Solids Struct.* **40**, 2501–2520.

Gonella S, Ruzzene M. (2008). Homogenization of vibrating periodic lattice structures. *Appl. Math. Model.* **32**, 459–482.

Gorbushin NA, Mishuris GS. (2018). Admissible steady-state regimes of crack propagation in a square-cell lattice. *Mech. Solids* **52**, 541–548.

Gourgiotis P, Georgiadis H, Neocleous I. (2013). On the reflection of waves in half-spaces of microstructured materials governed by dipolar gradient elasticity. *Wave Motion* **50**, 437–455.

Graff KF. (1975). *Wave motion in elastic solids.* Oxford University Press, Oxford.

Graff KF, Pao YH. (1967). The effects of couple-stresses on the propagation and reflection of plane waves in an elastic half-space. *J. Sound Vib.* **6**, 217–229.

Graffi T. (1946). *Memorie della Accademia delle Scienze.* Series 10, **4**, 103–109.

Haslinger SG, Movchan NV, Movchan AB, Jones IS, Craster RV. (2017). Controlling flexural waves in semi-infinite platonic crystals with resonator-type scatterers. *Quart. J. Mech. Appl. Math.* **70**(3), 216–247.

Hayes M, Rivlin RS. (1962). A note on the secular equation for Rayleigh waves. *ZAMP* **13**, 80–83.

Kaplunov J, Prikazchikov D. (2017). Asymptotic Theory for Rayleigh and Rayleigh-Type Waves. *Adv. Appl. Mech.* **50**, 1–106.

Kaplunov J, Prikazchikov D, Sultanova L. (2019). Rayleigh-type waves on a coated elastic half-space with a clamped surface. *Phil. Trans. R. Soc. A* **377**, 20190111.

Lee CH, Li G, Jin G, Liu Y, Zhang X. (2018). Topological dynamics of gyroscopic and Floquet lattices from Newtons laws. *Phys. Rev. B* **97**, 085110.

Linton CM, McIver M. (2002). The existence of Rayleigh-Bloch surface waves. *J. Fluid Mech.* **470**, 85–90.

Linton CM, Zalipaev V, Thompson I. (2013). Electromagnetic guided waves on linear arrays of spheres. *Wave Motion* **50**(1), 29–40.

Liu SW, Sung JC, Chang CS. (1996). Transient scattering of Rayleigh waves by surface-breaking and sub-surface cracks. *Int. J. Eng. Sci.* **34**, 1059–1075.

Long Y, Ren J, Chen H. (2018). Intrinsic spin of elastic waves. *PNAS* **115**, 9951–9955.

Marder M, Gross S. (1995). Origin of crack tip instabilities. *J. Mech. Phys. Solids* **43**, 1–48.

Mishuris GS, Slepyan LI. (2014). Brittle fracture in a periodic structure with internal potential energy. *Proc. R. Soc. A* **470**, 20130821.

Mitchell NP, Nash LM, Irvine WTM. (2018). Tunable band topology in gyroscopic lattices. *Phys. Rev. B* **98**, 174301.

Morini L, Piccolroaz A, Mishuris G, Radi E. (2013). On fracture criteria for dynamic crack propagation in elastic materials with couple stresses. *Int. J. Eng. Sci.* **71**, 45–61.

Morvaridi M, Carta G, Brun M. (2018). Platonic crystal with low-frequency locally-resonant spiral structures: wave trapping, transmission amplification, shielding and edge waves, *J. Mech. Phys. Solids* **121**, 496-516.

Nash LM, Kleckner D, Read A, Vitelli V, Turner AM, Irvine WTM. (2015). Topological mechanics of gyroscopic metamaterials. *Proc. Natl. Acad. Sci.* **112**, 14495–14500.

Nieves MJ, Movchan AB, Jones IS, Mishuris GS. (2013). Propagation of Slepyan's crack in a non-uniform elastic lattice. *J. Mech. Phys. Solids* **61**, 1464–1488.

Nieves MJ, Carta G, Jones IS, Movchan NV, Movchan AB. (2018). Vibrations and elastic waves in chiral multi-structures. *J. Mech. Phys. Solids* **121**, 387–408.

Nobili A, Radi E, Signorini C. (2020). A new Rayleigh-like wave in guided propagation of antiplane waves in couple stress materials. *Proc. R. Soc. A* **476**, 20190822.

Piccolroaz A, Gorbushin NA, Mishuris GS, Nieves MJ. (2020). Dynamic phenomena and crack propagation in dissimilar elastic lattices. *Int. J. Eng. Sci.* **149**, 103208.

Porter R, Evans DV. (1999). Rayleigh-Bloch surface waves along periodic gratings and their connection with trapped modes in waveguides. *J. Fluid Mech.* **386**, 233–258.

Porter R, Evans DV. (2005). Embedded Rayleigh-Bloch surface waves along periodic rectangular arrays. *Wave Motion* **43**(1), 29–50.

Rahman M, Barber JR. (1995). Exact expressions for the roots of the secular equation for Rayleigh waves. *J. Appl. Mech.* **62**, 250–252.

Rayleigh JWS. (1885). On waves propagated along the plane surface of an elastic solid. *Proc. London Math. Soc.* **17**, 4–11.

Slepyan LI. (2001). Feeding and dissipative waves in fracture and phase transition. III. Triangular-cell lattice. *J. Mech. Phys. Solids* **49**, 2839–2875.

Slepyan LI. (2002). *Models and Phenomena in Fracture Mechanics.* Springer, Berlin.

Slepyan LI. (2010). Dynamic crack growth under Rayleigh wave. *J. Mech. Phys. Solids* **58**, 636–655.

Süsstrunk R, Huber SD. (2015). Observation of phononic helical edge states in a mechanical topological insulator. *Science* **349**, 6243, 47–50.

Tomita S, Shindo Y. (1979). Rayleigh waves in magneto-thermoelastic solids with thermal relaxation. *Int. J. Eng. Sci.* **17**, 227–232.

Vinh PC, Giang PTH. (2010). On formulas for the Rayleigh wave velocity in pre-strained elastic materials subject to an isotropic internal constraint. *Int. J. Eng. Sci.* **48**, 275–289.

Vinh PC, Anh VTN. (2014). Rayleigh waves in an orthotropic half-space coated by a thin orthotropic layer with sliding contact. *Int. J. Eng. Sci.* **75**, 154–164.

Vinh PC, Hue TTT. (2014). Rayleigh waves with impedance boundary conditions in incompressible anisotropic half-spaces. *Int. J. Eng. Sci.* **85**, 175–185.

Viktorov IA. (1967). *Rayleigh and Lamb Waves.* Plenum Press, New York.

Wang P, Lu L, Bertoldi K. (2015). Topological phononic crystals with one-way elastic edge waves. *Phys. Rev. Lett.* **115**, 104302.

Wang C, Balogun O, Achenbach JD. (2019). Scattering of a Rayleigh wave by a near surface crack which is normal to the free surface. *Int. J. Eng. Sci.* **145**, 103162.

Zhao Y, Zhou X, Huang G. (2020). Non-reciprocal Rayleigh waves in elastic gyroscopic medium. *J. Mech. Phys. Solids* **143**, 104065.

Appendix A. Explicit solution for the phase velocity of Rayleigh waves in a non-gyroscopic continuum

Here, we present the explicit solution of (69), which gives the speed of Rayleigh waves on the surface of a continuum without gyricity. This solution is unexpectedly missing in many classical textbooks, and it was firstly published in closed form by Rahman & Barber (1995). The expression for the speed of Rayleigh waves will be given in a different and more concise form in the following; for a thorough study of the problem, the reader is encouraged to refer to the papers by Hayes & Rivlin (1962) and Rahman & Barber (1995).

Denoting the speed of Rayleigh waves by c_R and squaring both sides of (69), after some algebraic manipulations we obtain the expression

$$\frac{c_R^2}{c_s^2}\left[\frac{c_R^6}{c_s^6} - 8\frac{c_R^4}{c_s^4} + 24\frac{c_R^2}{c_s^2} - 16\frac{c_R^2}{c_p^2} + 16\left(\frac{c_s^2}{c_p^2} - 1\right)\right] = 0. \qquad (A.1)$$

By introducing the quantities $\mathcal{N} = (1 - \nu)/(1 - 2\nu) = c_p^2/(2c_s^2)$ and $Y = c_\mathrm{R}^2/c_s^2$, the equation (A.1) can be written in the form

$$Y\left[Y^3 - 8Y^2 + 8\left(3 - \frac{1}{\mathcal{N}}\right)Y + 8\left(\frac{1}{\mathcal{N}} - 2\right)\right] = 0\,. \qquad (A.2)$$

Since $Y = 0$ is not an admissible solution, we need to solve a cubic equation in Y.

The Poisson's ratio of linear isotropic elastic media lies in the range $(-1, 0.5)$. In this interval, the only acceptable solution $Y = c_\mathrm{R}^2/c_s^2$ is given by

$$\frac{c_\mathrm{R}^2}{c_s^2} = \frac{1}{3}\left[8 + \frac{2\sqrt[3]{2}(\mathcal{N} - 3)(1 + \mathrm{i}\sqrt{3})}{\sqrt[3]{f_1(\mathcal{N})}} - \frac{(1 - \mathrm{i}\sqrt{3})\sqrt[3]{f_1(\mathcal{N})}}{\sqrt[3]{2}\,\mathcal{N}}\right]$$
$$\text{for } -1 < \nu \le \frac{2}{5} \quad \left(\frac{2}{3} < \mathcal{N} \le 3\right)\,,$$

$$\frac{c_\mathrm{R}^2}{c_s^2} = \frac{1}{3}\left[8 - \frac{4\sqrt[3]{2}(\mathcal{N} - 3)}{\sqrt[3]{f_1(\mathcal{N})}} + \frac{\sqrt[3]{4}\sqrt[3]{f_1(\mathcal{N})}}{\mathcal{N}}\right] \qquad (A.3)$$
$$\text{for } \frac{2}{5} \le \nu < \frac{1}{2} \quad (3 \le \mathcal{N} < \infty)\,,$$

where

$$f_1(\mathcal{N}) = 45\,\mathcal{N}^2 - 34\,\mathcal{N}^3 + 3\sqrt{3}\sqrt{f_2(\mathcal{N})}\,, \qquad (A.4)$$
$$f_2(\mathcal{N}) = 44\,\mathcal{N}^6 - 124\,\mathcal{N}^5 + 107\,\mathcal{N}^4 - 32\,\mathcal{N}^3\,.$$

We note that $f_1(\mathcal{N}) < 0$ when $\mathcal{N} < 3$, while $f_1(\mathcal{N}) > 0$ when $\mathcal{N} > 3$. Furthermore, we observe that the cubic equation in (A.2) has three real roots for $\nu < \nu^*$ ($\mathcal{N} < \mathcal{N}^*$), where $\nu^* \simeq 0.263$ ($\mathcal{N}^* \simeq 1.555$) is a root of $f_2(\mathcal{N})/\mathcal{N}^3$.

The ratio c_R/c_s, given by the positive square root of (A.3), is plotted as a function of ν in Fig. A.1. We point out that for positive values of the Poisson's ratio, Fig. A.1 coincides with the diagram on the right of Fig. 6.8 in the book of Graff (1975).
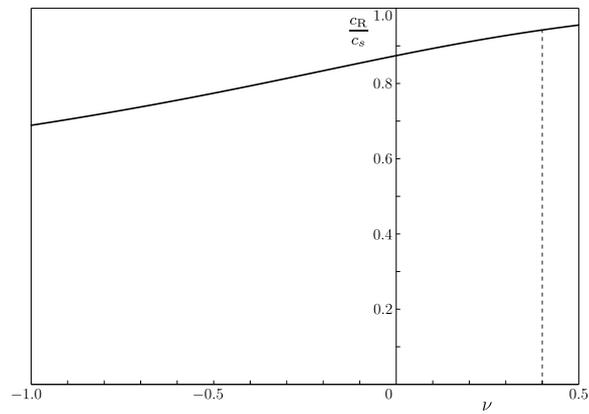
Figure A.1: Ratio between the speed of Rayleigh waves c_R and the speed of shear waves c_s, calculated in the interval $-1 < \nu < 0.5$. The vertical line $\nu = 0.4$ indicates the value of the Poisson's ratio where the expression of the ratio c_R/c_s changes (see (A.3)).

.